Chemical Science

Accepted Manuscript

This article can be cited before page numbers have been issued, to do this please use: C. Salguero and S. A. Lopez, *Chem. Sci.*, 2026, DOI: 10.1039/D6SC00969G.




ROYAL SOCIETY OF CHEMISTRY

rsc.li/chemical-science

View Article Online
DOI: 10.1039/D6SC00969G



# Singlet machine learning photodynamics reveal competing inversion paths of methylated cyclooctatetrathiophene

Christian Salguero and Steven A. Lopez*

Department of Chemistry and Chemical Biology, Northeastern University, Boston, Massachusetts, 02115, United States

*Corresponding author: s.lopez@northeastern.edu

## Abstract

We used state-of-the-art machine-learning nonadiabatic molecular dynamics to investigate the stereochemical inversion reaction of a methylated thiophene-fused cyclooctatetraene derivative, **MeCOTh**. Minimum energy path calculations suggest that the pseudo-dominant pathway of **MeCOTh** is towards a non-productive fluorescence decay pathway. Our machine learning photodynamics calculations revealed that relative stereochemical inversion occurs mainly on the $S_1$ surface (74% of trajectories), and we identified two competing inversion pathways. The first and main mechanistic pathway, seen in 62% of trajectories, showcases a “crown” structure with unidirectional sulfurs resulting from S-S closed-shell repulsions. The second pathway is the previously proposed inversion mechanism, which proceeds through a planar geometry of **MeCOTh**, and appeared in only 8% of trajectories. Our photodynamic simulations show that although excited-state Baird aromaticity contributes to the relative stereochemical inversion mechanism of **MeCOTh**, it is not the only electronic effect. Instead, the overall inversion mechanism is primarily governed by the interplay between Baird aromaticity and the S-S closed-shell repulsions.

## Introduction

Photochemistry exemplifies the principles of green chemistry by utilizing renewable solar energy to facilitate reactions under mild conditions while minimizing resource use and waste production. Light enables the precise activation of chemical processes, such as [2+2] cycloaddition reactions[1] and gas evolutions towards strained compounds (*e.g.,* cyclooctynes[2], tetrahedrane[3], and bicyclo[1.1.0]butane[4]), that would otherwise be thermally or kinetically unfavorable. The specific stereochemistry[5], efficient atom economy, and easy implementations[6] of these light-mediated reactions are of great interest in chemistry,[7-9] biology,[10-12] and material sciences[13-15]. Photochemical processes promote structural changes through isomerizations[16-18], bond breakage[19-21]/formation[22, 23] , and or electronic changes, such as the inversion of aromaticity[24-26]. This precise spatiotemporal control has enabled the applications of photochemical reactions in energy storage materials[1, 27, 28] and drug delivery[29-31].

Many organic chromophores feature conjugated $\pi$-systems; some of which are aromatic in the ground state. Aromaticity is a fundamental concept in chemistry that has evolved since its introduction in the 19th century.[32, 33] Aromatic compounds are exceptionally prevalent, with approximately two-thirds of all identified molecules exhibiting some aromatic component.[24, 33-35] The aromatic archetype, benzene, was first isolated in 1825 by Faraday. [36] Huckel presented his foundational work on aromaticity in 1931 using

View Article Online
DOI: 10.1039/D6SC00969G



molecular orbital theory to describe cyclic, π-conjugated hydrocarbons with '4n+2' π electrons as 'aromatic' [34, 37]. In 1965, Breslow built upon Huckel's '4n+2' rule by introducing the counter-concept of 'antiaromaticity,' which states that cyclic, π-conjugated hydrocarbons with '4n' π electrons are antiaromatic.[34, 38] In 1966, Dewar built on aromaticity studies by using perturbation molecular orbital theory to calculate and analyze the heat of formation energies of pairs of open-chain polyenes and their cyclic counterparts (*i.e.,* annulenes), offering qualitative evidence for the 4n+2 and 4n rules.[32, 39] In 1972, Baird conducted foundational research on excited-state aromaticity, identifying an inversion of Huckel's aromaticity rules in the triplet state (*i.e.,* antiaromatic structure: 4n+2 π and aromatic structure: 4n π).[40] Karadakov later extended this concept to the singlet excited state.[41, 42] In the last decade, Sung *et al.* and Oh *et al.* have successfully experimentally observed the reversal of aromaticity in the excited states of hexaphyrins using time-resolved infrared spectroscopy, providing experimental evidence for the existence of Baird's aromaticity.[43, 44]

Baird's excited-state aromaticity and antiaromaticity have been leveraged to create innovative photochemical reactions[26, 45-47] and photoresponsive materials[48-50], utilizing the principles of excited-state aromaticity[51, 52] or antiaromaticity relief. [53-55] Examples of these reactions include the photosolvolysis of 9-fluorenol[56] and cyclooctatetraene-fused acene dimers,[57, 58] as it stabilizes essential mechanistic structures in the excited-state surfaces that would be unstable in the ground-state surface.[24] In both instances, the ground-state ($S_0$) antiaromatic planar geometry of an intermediate[59] (such as the 4π-cationic intermediate)[56] or transition state (like the 8π cyclooctatetraene core)[57, 58, 60] adopts an aromatic electronic configuration in the excited state, thereby facilitating its respective reaction. Scheme 1 illustrates the excited-state aromatic 4π-cationic intermediate, which facilitates the hydroxy extraction from the 9-fluorenol.[24, 56]

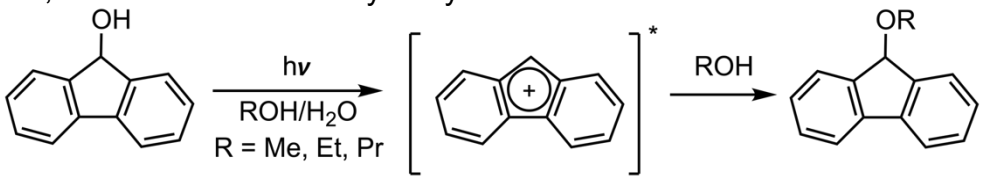


**Scheme 1.** Photosolvolysis of 9-fluorenol highlighting the stabilized aromatic 4π-cationic intermediate. [24, 56]

Cyclooctatetraene (**3**) was initially synthesized by Willstätter in 1911, sparking researchers' interest as it represented the next higher vinylogue of benzene.[61, 62] Unlike benzene, cyclooctatetraene (COT) has polyolefinic properties, adopting a tub geometry in the $S_0$ state rather than a planar geometry.[62, 63] As a 4n π system, its ground-state planar, bond-length equalized geometry ($D_{8h}$) is Huckel antiaromatic. Thus, the tub geometry is preferred to preclude the destabilizing conjugation of antiaromaticity.[42, 61-63]

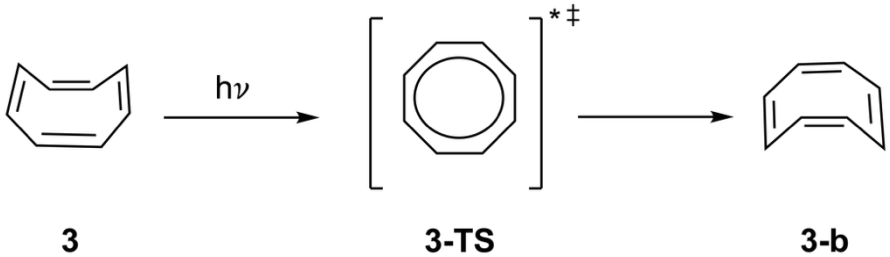

View Article Online
DOI: 10.1039/D6SC00969G



**Scheme 2.** Proposed excited-state inversion mechanism for cyclooctatetraene **(3)** through a planar transition state, **3-TS**, towards **3-b**.[17, 25, 64]

The $S_0$ interconversion from **3** to **3b** through a planar transition state (**3-TS**) was extensively studied and quantified to have a thermal barrier of approximately 10 kcal mol$^{-1}$.[24, 62, 65, 66] Previous studies have verified the planar, aromatic geometry of **3-TS** in the lowest triplet[67] and first singlet ($S_1$)[62, 68-70] excited states. Nonetheless, the impact of Baird aromaticity on the planarization energetics was unclear–**3** planarizes in a barrierless manner on the $S_1$-surface (Scheme 2).[25, 71] To explore the energetics of inversion and the contributions of Baird aromaticity, Ueda *et al.* synthesized and examined the inversion of a methylated thiophene fused derivative of **3**, **MeCOTh**.[25]

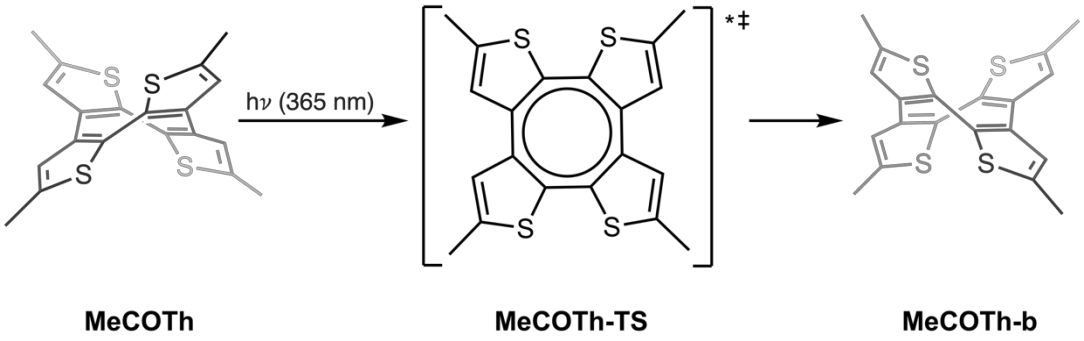


**Scheme 3.** Proposed excited-state inversion mechanism for methylated thiophene fused derivative of **3**, **MeCOTh**, through a planar transition state, **MeCOTh-TS**, towards the inverted geometry, **MeCOTh-b**.[25]

To provide experimental evidence for **MeCOTh** racemization, Ueda *et al.* used time-dependent circular dichroism to discover that **MeCOTh** could racemize thermally and photochemically.[25] The unirradiated samples showed no decrease in time-dependent circular dichroism signal, indicating that the reaction was light-mediated.[25] Time-resolved transient absorption spectroscopy identified only $S_1$ dynamics under λ = 365 nm irradiation, indicating selective $S_1$ excitation.[25] To evaluate the presence of Baird aromaticity in the $S_1$-state, **MeCOTh** was selectively promoted to the $T_1$-surface using a photosensitizer because Baird aromaticity is typically discussed in the triplet state.[25] This promotion facilitated a similar inversion, confirming the presence of Baird aromaticity on the $S_1$-surface.[25] The ground-state **MeCOTh** to **MeCOTh-b** inversion barrier was experimentally determined through circular dichroism decay profiles at temperatures of 40˚C, 50˚C, and 60˚C, and analyzed using the Eyring equation, resulting in a value of 25.4 kcal mol$^{-1}$.[25] Applying the same method at 0˚C, 10˚C, and 20˚C to the irradiated samples resulted in the $S_1$ and $T_1$ inversion barrier values of 4.3 kcal mol$^{-1}$ and 4.0 kcal mol$^{-1}$, respectively.[25] This shows a decrease of 21.1 kcal mol$^{-1}$ and 21.4 kcal mol$^{-1}$ in these inversion barriers compared to their ground-state counterpart.[25] Ueda *et al.* proposed that the lower $S_1$ and $T_1$ inversion barriers stem from Baird aromatic stabilization of the planar transition state accessed during inversion.[25] To provide proof, they utilized quantum

View Article Online
DOI: 10.1039/D6SC00969G



chemical calculations to investigate whether the photochemical planarization of **MeCOTh** is a consequence of Baird aromaticity.[25]

Density functional theory calculations with B3LYP-D3(BJ)/6–311+G(d,p)//B3LYP-D3(BJ)/6–31G(d) determine that the $S_0$ inversion barrier was 29.9 kcal mol$^{-1}$, exceeding the experimental value by 4.5 kcal mol$^{-1}$.[25] In line with this trend, calculations using TD-B3LYP-D3(BJ)/6–311+G(d,p)//B3LYP-D3(BJ)/6–31G(d) found that the inversion barriers for $S_1$ and $T_1$ were 8.6 kcal mol$^{-1}$ and 9.0 kcal mol$^{-1}$, respectively; these values were over-predicted by 4.3 kcal mol$^{-1}$ and 5.0 kcal mol$^{-1}$ compared to the experimental values.[25] The calculated inversion barriers matched experimental findings, showing substantial decreases in activation free energies (21.3 kcal mol$^{-1}$ and 20.9 kcal mol$^{-1}$ on the $S_1$ and $T_1$ surfaces, respectively).[25] This decrease was attributed to Baird aromatic stabilization of the planar transition state.[25] These calculations produce static structures of limited value for a photochemical reaction, where subnanosecond timescales severely limit molecular equilibration. Thus, nonadiabatic molecular dynamics simulations are crucial for revealing the reaction mechanism and establishing structure-reactivity correlations. Such calculations investigate various mechanistic pathways that **MeCOTh** accesses as it transitions between the key mechanistic points identified by Ueda *et al.*, enhancing their description of the inversion mechanism. We propose that Baird aromaticity promotes rapid inversions between **MeCOTh** and **MeCOTh-b** in the excited state and that the relative stereochemistries at the $S_1/S_0$ hopping points will remain in the final ground state geometries (*i.e.,* no further $S_0$ inversions).

We conducted a computational analysis of the inversion mechanism of **MeCOTh** through multiconfigurational (complete active space self–consistent field, CASSCF) and single-reference (time-dependent density functional theory, TD-DFT) quantum chemical calculations. In this study, we comprehensively outlined the reaction pathways for the inversion of **MeCOTh** to **MeCOTh-b** using our open-source machine learning code, Python rapid artificial intelligence ab-initio molecular dynamics (PyRAI$^2$MD)[72-74], which allowed us to perform machine-learned nonadiabatic molecular dynamics (ML-NAMD).

**Active space and characterization of excitation on the optimized global minimum**

The first step of the photochemical inversion reaction involves photon absorption to an electronically excited state. As such, we first computed the vertical excitation energies of **MeCOTh** with TD-DFT calculations using Gaussian16[75]. We compared our results to previous experimental studies that used a 365 nm light source (3.4 eV) to selectively promote **MeCOTh** to the $S_1$-state.[25] We performed vertical excitation energy calculations and characterized the nature of electronic transitions using range-separated hybrid functionals (*i.e.,* CAM-B3LYP[76] and ωB97X-D[77]) with a double-zeta basis set (*i.e.,* aug-cc-pVDZ[78, 79]). The predicted vertical excitation energy for the ground-state optimized **MeCOTh**, referred to as **MeCOTh-$S_0$**, was found to be 3.71 eV using CAM-B3LYP-D3(BJ)/aug-cc-pVDZ and 3.74 eV with ωB97X-D/aug-cc-pVDZ. Both approaches indicated that the $S_0 \rightarrow S_1$ excitation corresponds to a $\pi \rightarrow \pi^*$ transition in the COT-core, with oscillator strengths of 0.024 and 0.025, respectively. This consistent alignment with the experimental light source and TD-DFT calculations strongly validates our computational methods.

View Article Online
DOI: 10.1039/D6SC00969G



The multiconfigurational electronic structure of the **MeCOTh** during photoexcitation and photodynamic simulations requires multiconfigurational quantum mechanical techniques. Therefore, we employed CASSCF and complete active space second-order perturbation theory (CASPT2), both of which require an active space. We analyzed the orbital transitions suggested by TD-DFT and those relevant to the **MeCOTh** to **MeCOTh-b** isomerization (specifically, COT-core π orbitals). An active space comprising eight electrons was formulated across seven orbitals of the COT core; we excluded the highest-lying π*-orbital to prevent a double excitation to the $S_2$ state and enhance the efficiency of our computations (Figure 1).[80, 81]

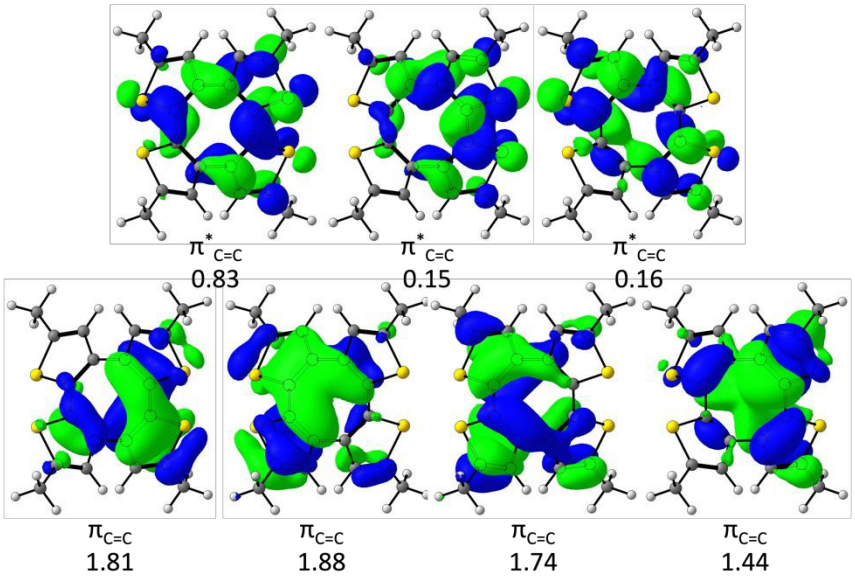


**Figure 1.** CASSCF(8,7) active space for **MeCOTh** consisting of eight electrons distributed within four π-orbitals and three π*-orbitals of the COT-core. We noted the average electron occupancy of each orbital below the respective orbital. An isosurface value of 0.03 was used for all orbital images.

To ensure accurate photophysical characterization using the (8,7) active space, we compared the vertical excitation energies and nature of transition predicted by TD-DFT, CASSCF, and CASPT2. The vertical excitation energy for **MeCOTh-$S_0$** was calculated using a state average of the first five singlet states (*i.e.,* $S_0$-$S_4$) for CASSCF (SA5-CASSCF(8,7)/ANO-S-VDZP) and applying the CASPT2 correction (CASPT2(8,7)/ANO-S-VDZP//SA5-CASSCF(8,7)/ANO-S-VDZP). We used a double-zeta basis set for all methods—aug-cc-pVDZ for TD-DFT and ANO-S-VDZP for CASSCF and CASPT2— to ensure that any observed differences between the methods stem from the treatment of electron correlation and not from basis set limitations. Both multiconfigurational methods overestimated the $S_0 \rightarrow S_1$ vertical excitation energy, reporting values of 5.72 and 4.22 eV, respectively, compared to the TD-DFT and experimental findings. The discrepancies observed in the CAS methods arise from the relatively small active space, which does not include all conjugated $\pi$-orbitals. Both methods classify this excitation as a π → π* transition within the COT core and align with the TD-DFT results. Table 1 presents a summary of these findings.

**Table 1**. Benchmarked TD-DFT and CASSCF vertical excitation energies.

| Method | State | Energy (eV) | Wavelength (nm) | Oscillator strength | Nature |
|---|---|---|---|---|---|
| | $S_1$ | 3.71 | 334 | 0.024 | π → π* |

View Article Online
DOI: 10.1039/D6SC00969G



| | | | | | |
|---|---|---|---|---|---|
| CAM-B3LYP-D3(BJ)/aug-cc-pVDZ | $S_2$ | 4.56 | 272 | 0.352 | π → π* |
| | $S_3$ | 4.82 | 257 | 0.139 | π → π* |
| | $S_1$ | 3.74 | 331 | 0.025 | π → π* |
| | $S_2$ | 4.60 | 270 | 0.376 | π → π* |
| | $S_3$ | 4.91 | 253 | 0.132 | π → π* |
| SA5-CASSCF(8,7)/ANO-S-VDZP | $S_1$ | 5.72 | 217 | 0.011 | π → π* |
| | $S_2$ | 6.62 | 187 | 0.112 | π → π* |
| | $S_3$ | 6.77 | 183 | 0.136 | π → π* |
| SA5-CASPT2(8,7)/ANO-S-VDZP// SA5-CASSCF(8,7)/ANO-S-VDZP | $S_1$ | 4.22 | 294 | | π → π* |
| | $S_2$ | 5.64 | 220 | | π → π* |
| | $S_3$ | 5.74 | 216 | | π → π* |

After we compared the orbital transitions, vertical excitation energies, and oscillator strengths between CASSCF, CASPT2, and TD-DFT, we concluded that CAS(8,7), as shown in Figure 1, appropriately captures the vertical excitation energies of **MeCOTh** at an equilibrium geometry on the ground-state (*i.e.*, **MeCOTh-$S_0$**). We used SA5-CASSCF(8,7)/ANO-S-VDZP for all subsequent calculations.

**Predicted absorption spectra and $S_1$ minimum energy path**

To verify that the (8,7) active space captures the spectral properties of **MeCOTh** at nonequilibrium geometries, we compute the absorption spectrum of **MeCOTh**; the computed and experimental (Ueda *et al.*[25]) spectra are compared. To that end, we generate 500 Wigner-sampled non-equilibrium structures based on the frequencies of **MeCOTh-$S_0$** (Figure 2a) and computed the vertical excitation energies [$S_0 \rightarrow S_n$ (n=1-4)] and oscillator strengths for each structure with MS-CASPT2(8,7)/ANO-S-VDZP//SA(5)-CASSCF(8,7)/ANO-S-VDZP (Figure 2b).[82] The reported experimental spectrum[25] spanned a range of 200 to 500 nm, showing peaks at approximately 270 nm and 230 nm, with notable absorption at 300 nm that drops off to a low-absorption tail beyond 350 nm.[25] Therefore, we only plotted the peaks above 200 nm for direct comparison with the experimental absorption spectrum. The intensities of the calculated spectrum are normalized using the $S_0 \rightarrow S_3$ transition. All experimental investigations of the **MeCOTh** → **MeCOTh-b** inversion dynamics utilized a light source of 365 nm to selectively excite **MeCOTh** to the $S_1$ surface using the longest wavelength absorption band.[25]

View Article Online
DOI: 10.1039/D6SC00969G



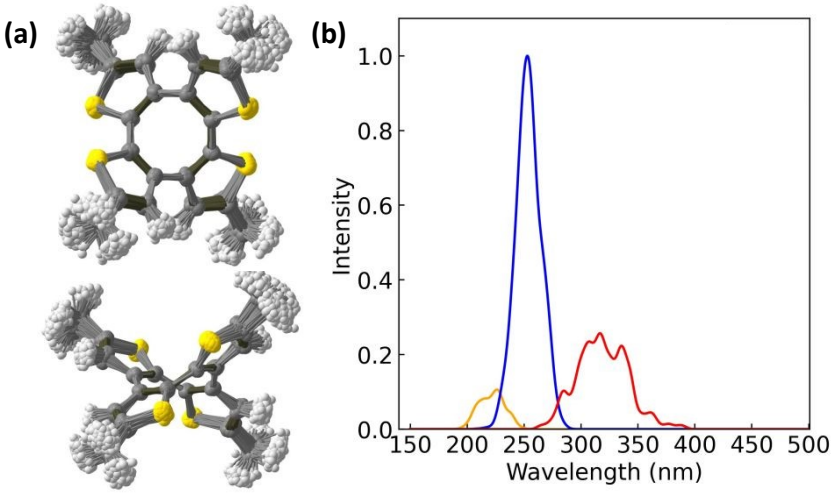


**Figure 2.** (a) The top view (top) and side view (bottom) overlay of 500 non-equilibrium structures from the Wigner ensemble of **MeCOTh**. (b) The predicted absorption spectrum was generated by aggregating the 500 vertical excitation energy calculations. The absorption intensity is normalized to the peak with the highest oscillator strength, $S_3$. All calculations utilized the MS-CASPT2(8,7)/ANO-S-VDZP//CASSCF(8,7)/ANO-S-VDZP method.[82]

The computed spectrum (Figure 2b) shows three absorption peaks centered at 317 nm, 253 nm, and 226 nm, corresponding to π→π* transitions. The $S_0 \rightarrow S_3$ transition is represented by the yellow peak centered at 226 nm, which is the lowest-intensity peak. The blue peak, centered at 253 nm, corresponds to the $S_0 \rightarrow S_2$ transition and has the highest intensity of all three peaks (*i.e.,* the bright state). The red peak centered at 317 nm has the second-highest intensity and corresponds to the lowest-energy transition, $S_0 \rightarrow S_1$; it features a low-absorption tail extending above 350 nm and diminishing completely by 400 nm. While the intensity of $S_0 \rightarrow S_2$ is higher than the intensity of the $S_0 \rightarrow S_1$ transition, the $S_0 \rightarrow S_2$ transition cannot be accessed using the experimental light source (365 nm) because the excitation energy required exceeds the energy of the photon source.

To assess the accuracy of our computed spectrum, we matched the observed peaks in the computed spectrum to those observed in the experimental spectrum; matching peaks and spectral shapes between the experimental and computed spectra would indicate that our electronic structure method (MS-CASPT2(8,7)/ANO-S-VDZP//CASSCF(8,7)/ANO-S-VDZP) captures the spectral properties of **MeCOTh** correctly. The highest-intensity peak in the experimental spectrum is at approximately 230 nm, whereas the highest-intensity peak in the computed spectrum is at 253 nm (*i.e.,* the $S_0 \rightarrow S_2$ peak). This indicates that the computed spectrum is redshifted by 23 nm relative to the highest-intensity peak of the experimental spectrum. The second-highest-intensity peak in the experimental spectrum is at approximately 270 nm, whereas in the computed spectrum it is at 317 nm (*i.e.,* the $S_0 \rightarrow S_1$ peak). Like the $S_0 \rightarrow S_2$ peak, the corresponding $S_0 \rightarrow S_1$ peak is also red-shifted (62 nm) in the computed spectra relative to the peak observed experimentally.[25] The experimental spectrum shows significant absorption between the two peaks (*i.e.,* between 230 and 270 nm).[25] This region matches the

View Article Online
DOI: 10.1039/D6SC00969G



calculated overlap region that we observed between the $S_0 \rightarrow S_1$ and $S_0 \rightarrow S_2$ transition peaks (250 to 300 nm). After the peak at 270 nm, the experimental spectrum exhibits a shoulder region with significant absorption that drops into a low-absorption tail beyond 350 nm, which is used to selectively excite **MeCOTh** to the $S_1$ state.[25] Our calculated $S_0 \rightarrow S_1$ peak at 317 nm has a low-absorption tail extending beyond 350 nm, matching the tail observed in the experiment.[25] The experimental spectrum has decreased absorption at higher wavelengths (*i.e.,* < 230 nm). In our computed spectra, the $S_0 \rightarrow S_3$ peak has the lowest intensity and shows significant overlap with the $S_0 \rightarrow S_2$ peak; both $S_0 \rightarrow S_2$ and $S_0 \rightarrow S_3$ peaks decrease in intensity at higher wavelengths. Based on these results, we conclude that the calculated spectrum has peaks that are consistently redshifted (*i.e.,* by +17 nm and +47 nm for $S_0 \rightarrow S_n$ (n=1-2), respectively) compared to those present in the experimental spectrum reported by Ueda *et al*.[25] The discrepancy between $\lambda^{max}$ and intensities can be attributed to the limitations of CASPT2 (*e.g.,* a MAE of 0.11 eV[83, 84] ), basis set effect[84, 85], and to a relatively small active space that does not include all conjugated $\pi$-orbitals.

After assessing the spectral properties, we shifted our focus to elucidating the mechanism of the photochemical reaction. Given that the $S_1$ state is the only energetically accessible excited state under the experimental light source,[25] we calculated the minimum energy path (MEP) to identify the steepest descent path along the $S_1$ surface, starting from the Franck-Condon point of **MeCOTh-$S_0$**. We hypothesize that **MeCOTh** will adopt a more planar structure along $S_1$-MEP, with uniform bond lengths in the COT core (*i.e.,* $\pi_{CC}$ and $\sigma_{CC}$) because the core is Baird aromatic on the $S_1$-state, favoring a planar confirmation for maximal π-orbital overlap. Figure 3 shows the $S_1$-MEP, the **MeCOTh-$S_0$** geometry, the final MEP step geometry (**MeCOTh-MEP-11**), and an $S_1$ minimum geometry (**MeCOTh-$S_1$**).

View Article Online
DOI: 10.1039/D6SC00969G



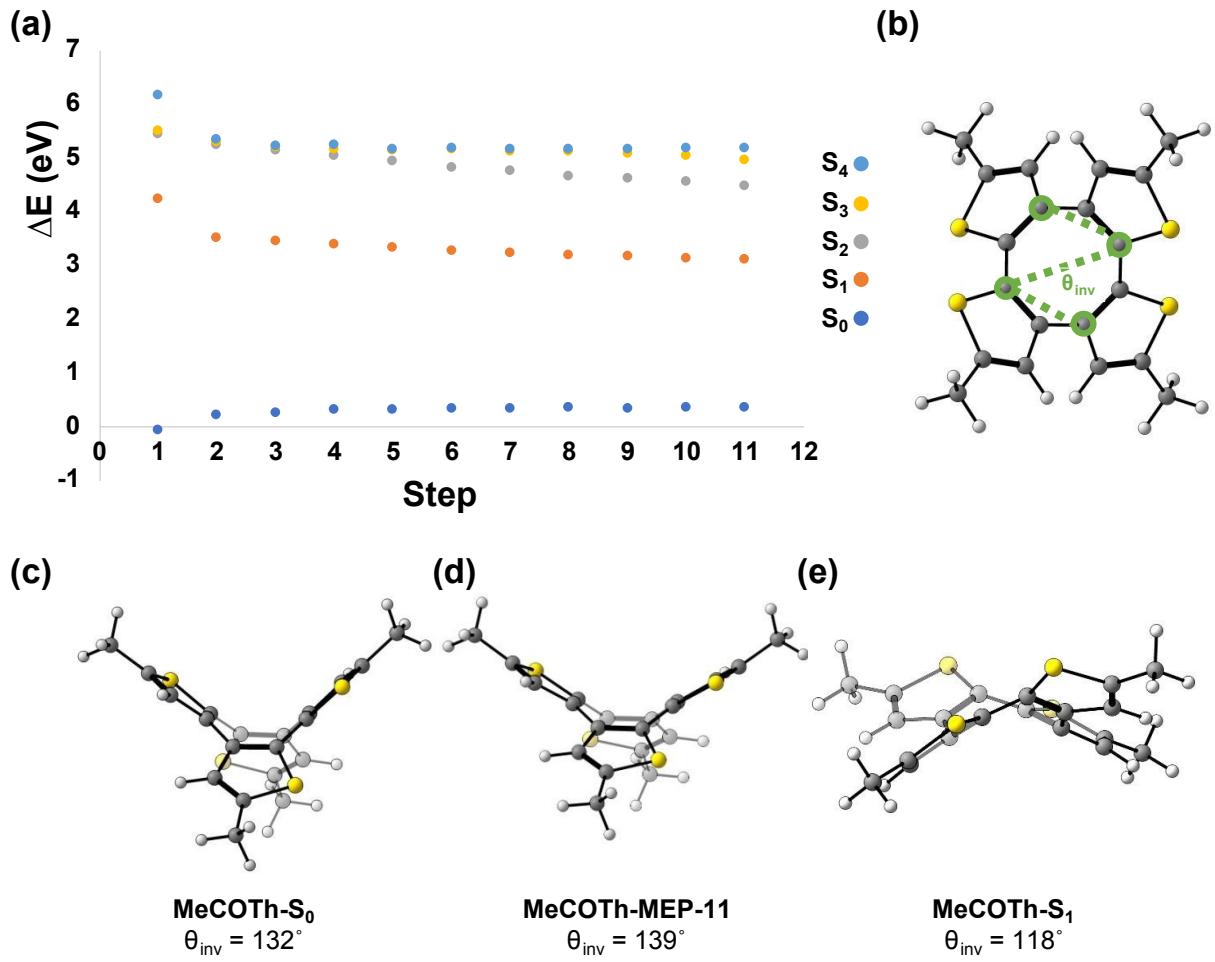


**Figure 3.** (a) The calculated MEP of **MeCOTh** along the $S_1$ surface at the SA(5)-CASPT2(8,7)/ANO-S-VDZP level. (b) The defined inversion angle, $\theta_{inv}$, includes $C_1$-$C_9$-$C_4$-$C_6$, which are highlighted in green. We used $\theta_{inv}$ to monitor the planarization of the COT core. The bottom structures correspond to (c) the ground state, optimized SA(5)-CASPT2(8,7)/ANO-S-VDZP, **MeCOTh-$S_0$**, (d) the final step of MEP, **MeCOTh-MEP-11**, and (e) the optimized $S_1$ minimum, **MeCOTh-$S_1$.** All energies are relative to the ground-state-optimized geometry, **MeCOTh-$S_0$**.

Figure 3a illustrates the MEP along the $S_1$ surface and the energies corresponding to the $S_0$-$S_4$ states; it includes 11 geometries. The $S_1$-MEP converges to a structure 3.11 eV (**MeCOTh-MEP-11**) above the **MeCOTh-$S_0$**. At **MeCOTh-MEP-11**, the $S_1/S_0$ energy gap is 2.74 eV; this large $S_1$-$S_0$ energy gap provides a direct path to a radiative decay channel. Figures 3c-e show three geometries: **MeCOTh-$S_0$**, **MeCOTh-MEP-11**, and **MeCOTh-$S_1$**. We defined a planarity parameter, $\theta_{inv}$, within the COT core to quantify the change in planarity within these three geometries and along the MEP (Figure 3b); at a perfectly planar geometry, $\theta_{inv}$ would be 180˚. **MeCOTh-$S_0$** and **MeCOTh-MEP-11** have $\theta_{inv}$ values of 132˚ and 139˚, respectively (Figures 3c and 3d). There is an increase of 7˚ in $\theta_{inv}$ from **MeCOTh-$S_0$** → **MeCOTh-MEP-11**; the rise in $\theta_{inv}$ indicates increased planarity in **MeCOTh** along the $S_1$ surface as it approaches 180˚. We assessed the bond lengths of $\pi_{CC}$ and $\sigma_{CC}$ in the COT core to investigate the bond length equalization that occurs

View Article Online
DOI: 10.1039/D6SC00969G



concurrently with aromatic systems. The four $\pi_{CC}$ measured 1.38 Å, 1.37 Å, 1.35 Å, and 1.37 Å while $\sigma_{CC}$ bonds measured 1.47 Å, 1.48 Å, 1.47 Å, and 1.47 Å at **MeCOTh-S$_0$.** At **MeCOTh-MEP-11**, the $\pi_{CC}$ measured 1.41 Å, 1.43 Å, 1.42 Å, and 1.41 Å, while the $\sigma_{CC}$ measured 1.39 Å, 1.41 Å, 1.40 Å, and 1.41 Å. We find that all $\pi_{CC}$ bond lengths have increased while all $\sigma_{CC}$ bond lengths have decreased. This bond equalization coincides with an increase in planarization. Both geometric changes suggest that the electronic structure of **MeCOTh-S$_0$** becomes Baird aromatic, consistent with our initial hypothesis.

We optimized an $S_1$ minimum, **MeCOTh-S$_1$**, using the final MEP geometry as an input (Figure 3e). **MeCOTh-S$_1$** is 2.65 eV above **MeCOTh-S$_0$** and has a $\theta_{inv}$ value of 118˚. This indicates a decrease of 14˚ and 21˚ from **MeCOTh-S$_0$** and **MeCOTh-MEP-11**, respectively. The decreased $\theta_{inv}$ corresponds to a less planar structure than **MeCOTh-S$_0$** or **MeCOTh-MEP-11**. We then measured the $\pi_{CC}$ and $\sigma_{CC}$ bond lengths to directly compare to **MeCOTh-S$_0$** and **MeCOTh-MEP-11**. In **MeCOTh-S$_1$**, the four $\pi_{CC}$ bonds measured 1.44 Å, 1.45 Å, 1.44 Å, and 1.45 Å, while the four $\sigma_{CC}$ bonds measured 1.39 Å, 1.39 Å, 1.37 Å, and 1.40 Å. The elongated $\pi_{CC}$ and shortened $\sigma_{CC}$ indicate a double bond shift within the COT core. The decrease in $\theta_{inv}$ and the double bond shift resulted in a conformational change from a tub geometry in **MeCOTh-S$_0$** and **MeCOTh-MEP-11** to a boat-boat conformation[86] in **MeCOTh-S$_1$**. After $S_1$ optimization, the $S_1/S_0$ gap in **MeCOTh-S$_1$** is 0.30 eV. The small $S_1/S_0$ gap suggests that the steepest path of descent is nonradiative, but it does not specify whether a relative stereochemical inversion occurs. While the MEP calculation provides detailed information on a single, steepest $S_1$ pathway, it omits dynamic information about the inversion mechanism.

We addressed the omitted dynamical effects by performing ML-NAMD simulations based on multiconfigurational quantum mechanical calculations. We generated 988 initial conditions via the Wigner sampling algorithm for production trajectories based on the frequencies of the **MeCOTh-S$_0$**. We captured nonadiabatic transitions (*i.e.,* surface hops) using the fewest-switches surface hopping (FSSH) algorithm[87] for 5.5 ps with curvature-driven time-derivative coupling (*k*TDC) to evaluate nonadiabatic coupling based on the energy gaps predicted by the neural networks (NNs).[88, 89] After 5.5 ps, 947 (96%) trajectories were on the $S_0$-state, while 41 (4%) were on the $S_1$-state. Based on the findings by Ueda *et al.*, we hypothesize that longer excited-state lifetimes may lead to increased stereochemical inversions, owing to the reduced $S_1$-state inversion barrier. The increased inversions would directly affect the relative stereochemistries of the final geometries of the trajectories. In Figure 4, we analyzed the relative stereochemistries of all trajectories by monitoring $\theta_{inv}$. We tracked the $\theta_{inv}$ values until the final $S_1/S_0$ crossings, extending each trajectory by 500 fs on the $S_0$ surface (*i.e.,* after the $S_1/S_0$ hop). This 500-fs window was set to ensure that the trajectories completely adopted their corresponding relative stereochemistries after the last $S_1 \rightarrow S_0$ hop (indicated by black dots), preventing ground-state inversions. Thus, the total length of our trajectories varies and is directly related to their respective excited-state lifetime. After the 500-fs duration on the $S_0$ surface, we classified the trajectories according to their final geometry and plotted their respective $\theta_{inv}$ as a function of simulation time (ps) in Figure 4.

View Article Online
DOI: 10.1039/D6SC00969G



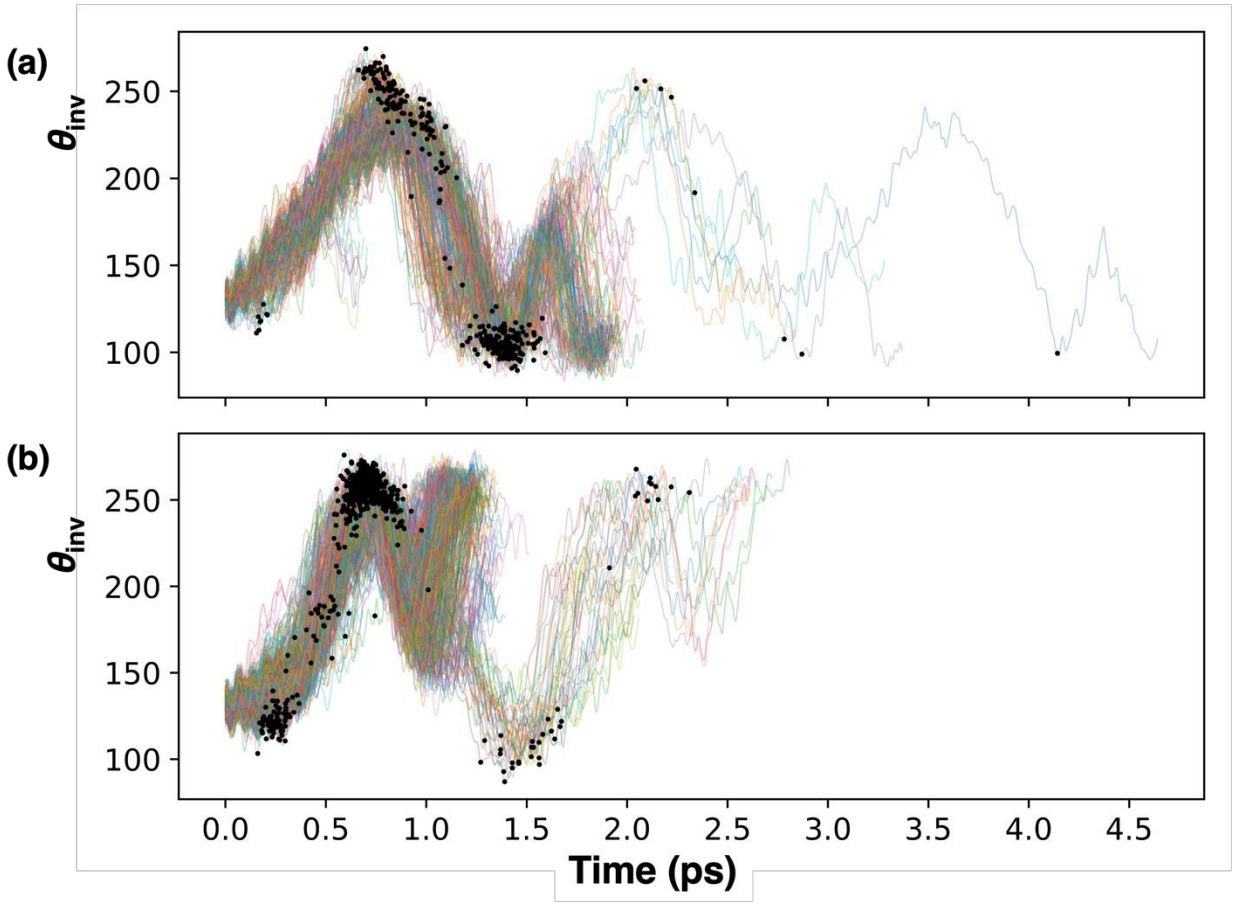


**Figure 4.** Trajectory map ($\theta_{inv}$ vs. simulation time) of **MeCOTh** → **MeCOTh-b** inversion. We separated the trajectories based on the geometry 500 fs after the $S_1/S_0$ crossing (a) retained, **MeCOTh**, and (b) inverted, **MeCOTh-b**. Black dots represent $S_1/S_0$ surface hopping points.

The optimized geometry, **MeCOTh-$S_0$**, has a $\theta_{inv}$ of 132˚. Thus, we labeled structures with $\theta_{inv}$ < 180˚ as having retained relative stereochemistries (**MeCOTh**) when compared to **MeCOTh-$S_0$** (Figure 4a). Structures with $\theta_{inv}$ > 180° are labeled as having inverted relative stereochemistries (**MeCOTh-b**) when compared to **MeCOTh-$S_0$** (Figure 4b). We observed that 304 trajectories led to **MeCOTh** (Figure 4a), while 643 led to **MeCOTh-b** (Figure 4b). Trajectories leading to **MeCOTh** have an average simulation time of 1.7 ps (Figure 4a), while trajectories leading to **MeCOTh-b** have an average simulation time of 1.2 ps (Figure 4b). On average, trajectories leading to **MeCOTh** were on the $S_1$ surface 0.5 ps longer than those leading to **MeCOTh-b**. The difference in simulation time demonstrates that longer excited-state lifetimes increase the probability of inversions; at least two inversions are required to revert to **MeCOTh**.

We defined two torsional regions in Figure 4 that represent the relative stereochemistries of **MeCOTh** ($\theta_{inv}$ < 180˚) and **MeCOTh-b** ($\theta_{inv}$ > 180˚). Trajectories in which the $\theta_{inv}$ values transition from less than 180° to over 180°, or vice versa, undergo a relative stereochemistry inversion. To quantify the relative stereochemical inversions in the excited state, we measured the average simulation time—directly linked to the excited-state lifetime—of the trajectories shown in Figures 4a and 4b, along with the $\theta_{inv}$

View Article Online
DOI: 10.1039/D6SC00969G



transitions across these regions. We expected either no inversions or an even number of stereochemical inversions (*i.e.,* $\theta_{inv}$ crossing from and to 180˚) in Figure 4a for trajectories leading to **MeCOTh**; a single or an odd number of relative stereochemical inversions is expected for trajectories that yield **MeCOTh-b** (Figure 4b). In Figure 4a, we observe that trajectories had an average simulation time of 1.7 ps and a maximum of 6 relative stereochemical inversions (*i.e.,* $\theta_{inv}$ crossing from and to 180˚). In Figure 4b, we observe that trajectories had an average simulation time of 1.2 ps and a maximum of 3 relative stereochemical inversions (*i.e.,* $\theta_{inv}$ crossing from and to 180˚). From these findings, we concluded that a longer duration in the $S_1$ state promotes more inversions, as shown in Figure 4a, where trajectories leading to **MeCOTh** require 2 or more inversions and remain, on average, 0.5 fs longer in the excited state. In contrast, trajectories that lead to **MeCOTh-b** remain on the excited state for shorter durations and have fewer inversions. These results are consistent with Ueda *et al.*, who found that the barrier for relative stereochemical inversion in the excited state is 4.3 kcal $mol^{-1}$, due to Baird aromaticity, which facilitates the relative stereochemical inversion.[25]

## Hopping Point Analysis

We investigate the retention of relative stereochemistry and the prevalence of $S_0$-inversions by comparing the relative stereochemistries at $S_1/S_0$ hopping points and final geometries. We anticipate that the relative stereochemistries at the $S_1/S_0$ hopping points will align with the relative stereochemistries of the final geometries of the trajectories. (*i.e.,* no $S_0$-state inversion). We plotted the $S_1/S_0$ hopping points against time in Figure 5. A trajectory analysis reveals that **MeCOTh** can undergo one or more surface hops; thus, for clarity, we restricted the depicted hopping points to the final $S_1 \rightarrow S_0$ hop, totaling 947 hopping points in Figure 5. We use $\theta_{inv}$ to assess the relative stereochemistries of the $S_1/S_0$ hopping points.

View Article Online
DOI: 10.1039/D6SC00969G



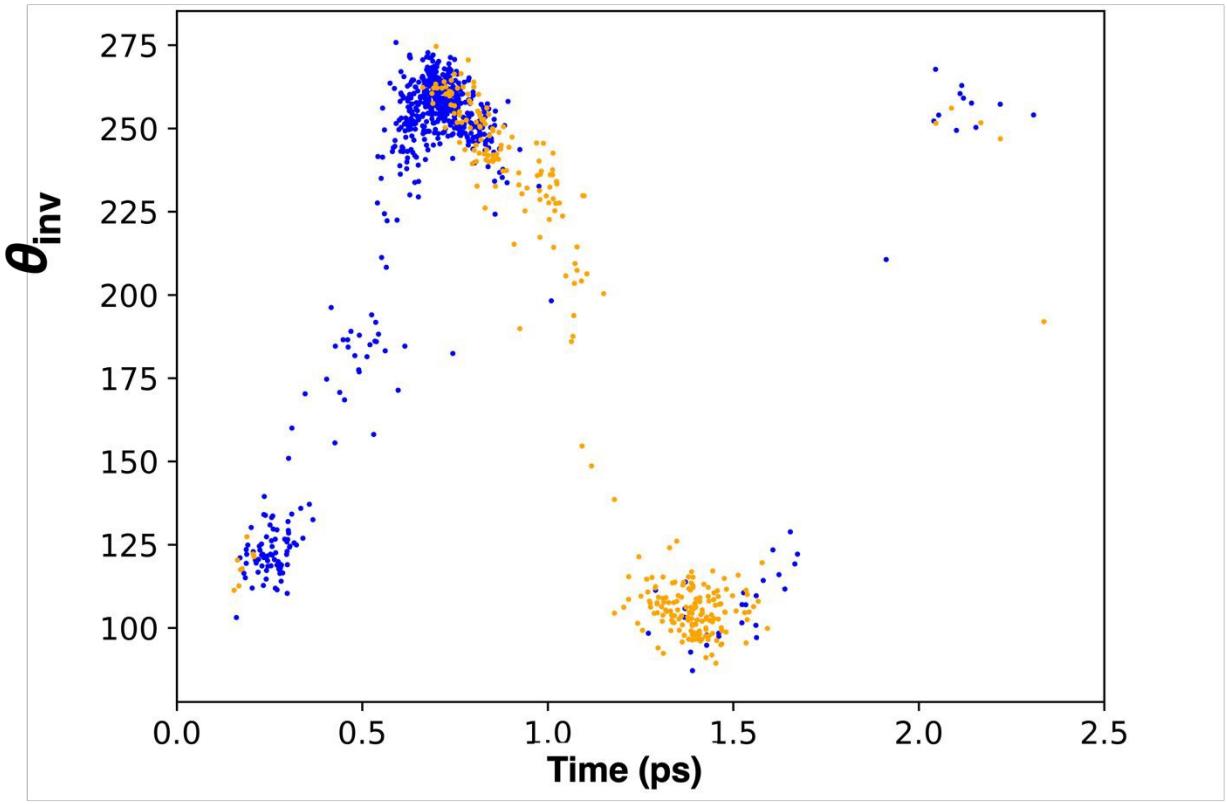


**Figure 5.** We implement color coding for the hopping points according to their relative stereochemistry 500 fs after $S_1 \rightarrow S_0$ relaxation: orange denotes the relative stereochemistry of **MeCOTh**, and blue represents the relative stereochemistry of **MeCOTh-b.**

In Figure 5, we identify three clusters of hopping points: 0 – 0.5 ps, 0.501 – 1 ps, and above 1.01 ps, which we have labeled based on their timing as "early," "intermediate," and "late." The early cluster comprises 103 hopping points in the torsional region pertaining to the relative stereochemistry of **MeCOTh** ($\theta_{inv} < 180^{\circ}$). Within this cluster, 95 (92%) of the hopping points belong to trajectories leading to **MeCOTh-b**, while 8 (8%) are associated with trajectories that yield **MeCOTh**. The relative stereochemistry of the main product, **MeCOTh-b** ($\theta_{inv} = 228°$), differs from the relative stereochemistry associated with the torsional region occupied by the early cluster (*i.e.,* $\theta_{inv} < 180^{\circ}$). This finding contradicts our hypothesis; we expected that the relative stereochemistries of $S_1/S_0$ hopping points would align with those of the final geometries. The difference in relative stereochemistries between the $S_1/S_0$ hopping points and the final geometries within this cluster results from the $S_1/S_0$ crossings having increased momentum, which leads to the second relative stereochemical inversion of **MeCOTh** on the $S_0$ state (*i.e.,* no retention of relative stereochemistries; Figure S7).

The intermediate cluster includes 613 hopping points within the torsional region corresponding to **MeCOTh-b** ($\theta_{inv} > 180^{\circ}$). The intermediate cluster has 510 hopping points (83%) that belong to trajectories that lead to **MeCOTh-b**, while the remaining 103 hopping points (17%) are associated with trajectories yielding **MeCOTh**. In contrast to the early cluster, the relative stereochemistry of the major product from the intermediate cluster, **MeCOTh-b** ($\theta_{inv} = 228^{\circ}$), aligns with the relative stereochemistry associated with

View Article Online
DOI: 10.1039/D6SC00969G



the conformational region occupied by that cluster (*i.e.,* $\theta_{inv}$ > 180˚). This finding indicates that the main pathway within the intermediate cluster leads to the relative stereochemistries at the $S_1/S_0$ hopping points remaining consistent in the final structures, supporting our initial hypothesis and previous work.[25]

The late cluster contains 231 hopping points in the torsional region of **MeCOTh** ($\theta_{inv}$ < 180˚). Within this cluster, 38 hopping points (16%) belong to trajectories leading to **MeCOTh-b,** and 193 hopping points (84%) belong to trajectories leading to **MeCOTh**. The main product of the late cluster, **MeCOTh** ($\theta_{inv}$ = 132˚), is located within the torsional region occupied by this cluster. This finding indicates that the main pathway within the late cluster leads to conserving the relative stereochemistries of the $S_1/S_0$ hopping points. We conclude that the preserved relative stereochemistries between the $S_1/S_0$ hopping points of the intermediate and late clusters and the final geometries of their trajectories result from the **MeCOTh** fully adopting the relative stereochemistries of $S_1/S_0$ hopping points on the $S_1$ state and transitioning to the $S_0$ surface afterward. Consequently, the inversion barrier increases to 25.4 kcal $mol^{-1}$,[25] preventing ground-state reinversion. Relative stereochemistry conservation is absent in the trajectories that undergo $S_1 \rightarrow S_0$ crossings within the early cluster, as trajectories that undergo early hopping have increased momentum relative to trajectories that undergo surface hopping at later timesteps (*i.e.,* intermediate and late clusters) due to the initial relaxation from the Franck-Condon region (Figure S8), affording the $S_0$ inversion from **MeCOTh** to **MeCOTh-b**.

To investigate the structural diversity within the clusters of surface-hopping points, we optimized three minimum-energy conical intersections (MECIs) for each relative stereochemistry (*i.e.,* **MeCOTh** and **MeCOTh-b**), using the $S_1/S_0$ hopping points as initial guess structures. We hypothesize that the optimized MECIs of trajectories leading to **MeCOTh** and **MeCOTh-b** will be stereoisomers of one another, and that trajectories with $S_1/S_0$ hopping points exhibiting opposite relative stereochemistries compared to their final geometries might optimize to different MECI than those with matching relative stereochemistries. To test these hypotheses, we use $\theta_{inv}$ to assess the relative stereochemistries of the $S_1/S_0$ hopping points. Figure 6 shows the differences in geometries and $\theta_{inv}$ for three representative MECIs- **MeCOTh-MECI-early, MeCOTh-MECI-intermediate**, and **MeCOTh-MECI-late**- and the three previously defined mechanistic critical points.

View Article Online
DOI: 10.1039/D6SC00969G



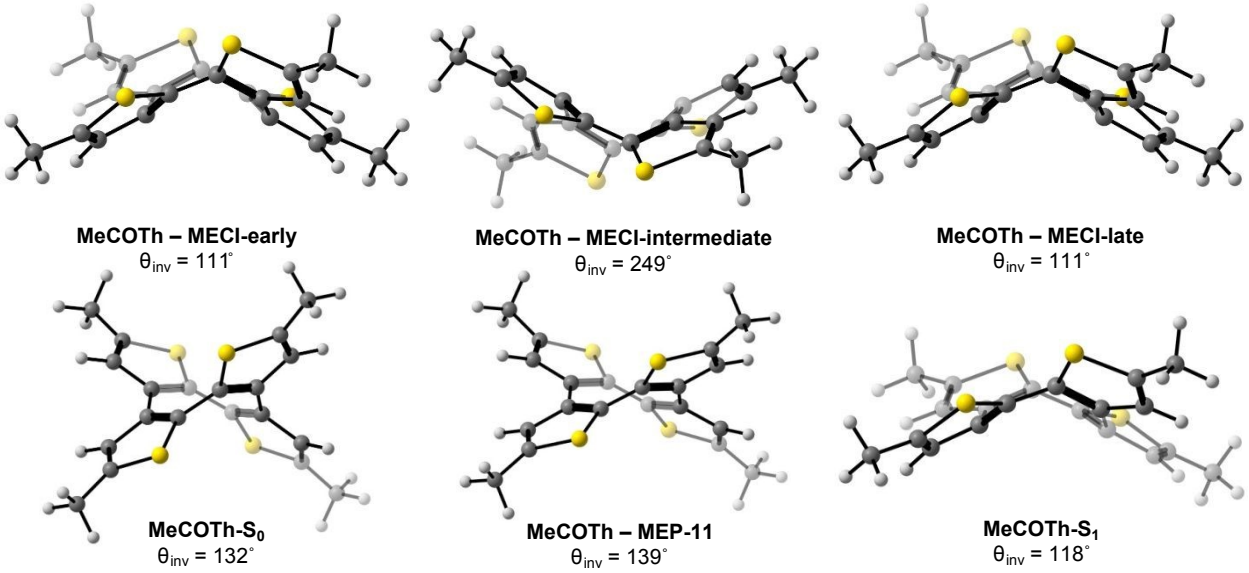


**Figure 6**. We compared an SA5-CASSCF(8,7)/ANO-S-VDZP optimized minimum energy conical intersections from each cluster: **MeCOTh-MECI-early**, **MeCOTh-MECI-intermediate**, and **MeCOTh-MECI-late** to **MeCOTh-S$_0$**, **MeCOTh-MEP-11**, **MeCOTh-S$_1$**. Each structure has their inversion angle, $\theta_{inv}$, below.

All optimized MECIs from $S_1/S_0$ hopping points in the early and late clusters have a $\theta_{inv}$ of 111°, regardless of the final geometry (**MeCOTh** or **MeCOTh-b**). This $\theta_{inv}$ value indicates that the relative stereochemistries of these MECIs correspond to **MeCOTh**. In contrast, all MECIs optimized from $S_1/S_0$ hopping points in the intermediate cluster had $\theta_{inv}$ = 249°, irrespective of the relative stereochemistries of the final geometry. This $\theta_{inv}$ value indicates that these MECIs have relative stereochemistries matching **MeCOTh-b**. Regardless of the cluster or the final relative stereochemistry, all MECIs remained at 3.25 eV above **MeCOTh-S$_0$** (see Table S1 for all optimized MECIs).

To assess whether the optimized MECIs are structurally equivalent, we compared their bond lengths ($\pi_{CC}$ and $\sigma_{CC}$) within the COT core and $\theta_{inv}$ to each other, as well as to other key mechanistic points (*i.e.,* **MeCOTh-S$_0$**, **MeCOTh-MEP-11**, and **MeCOTh-S$_1$**; Figure 6). In Figure 6, **MeCOTh-S$_0$** and **MeCOTh-MEP-11** have tub geometries with $\theta_{inv}$ values of 132˚ and 139˚, respectively. In contrast, **MeCOTh-MECI-early**, **MeCOTh-MECI-intermediate**, **MeCOTh-MECI-late**, and **MeCOTh-S$_1$** have boat-boat geometries with $\theta_{inv}$ values of 111˚, 249˚, 111˚, and 118˚, respectively. All $\pi_{CC}/\sigma_{CC}$ bond lengths remain consistent in all optimized MECIs (Table S1). The consistent $\pi_{CC}/\sigma_{CC}$ bond lengths, boat-boat conformation, and comparable energies across all optimized MECIs imply that MECIs within each cluster are the same. Furthermore, the MECIs optimized from the early/late clusters are stereoisomers of those from the intermediate cluster. The similar $\pi_{CC}/\sigma_{CC}$ bond lengths and shared conformation between MECIs and **MeCOTh-S$_1$** indicate these structures occupy similar regions of the potential energy surface. The findings show no alternative MECI in the clusters for trajectories with opposite relative stereochemistries between the $S_1/S_0$ hopping points and their final geometries. Therefore, an $S_0$ inversion must take place in these trajectories.

Figures 4 and 5 illustrate $\theta_{inv}$ against simulation time in picoseconds. We observed that all trajectories increase from $\theta_{inv}$ = 132˚ (**MeCOTh**) to $\theta_{inv}$ = 228˚ (**MeCOTh-b**) within

View Article Online
DOI: 10.1039/D6SC00969G



1 ps. This increase in $\theta_{inv}$ suggests that within the trajectories of **MeCOTh** → **MeCOTh-b**, a structure must exist where $\theta_{inv}$ = 180˚ (*i.e.,* a planar cyclooctatetraene core). This illustration of the ensemble of ML-NAMD trajectories (Figure 4) agrees with the MEP (Figure 3a); the **MeCOTh** planarizes. We hypothesized that the dominant inversion mechanism is facilitated by a planar structure, which is supported by the findings of Ueda *et al.*[25], our MEP (Figure 3a), and the ML-NAMD trajectory maps (Figure 4).

We defined new geometric parameters about the COT core to capture the planarity more accurately due to $\pi_{CC}$-torsions (Figure 7). We define angles $\theta_{1\text{-}4}$ to characterize the torsions resulting from the concomitant rotation of any two thiophenes, while angles $\theta_{5\text{-}8}$ are assigned to capture the torsions within the thiophenes. In an ideal planar geometry, all angles ($\theta_{1\text{-}8}$) should fall within ± 20˚ of the angles that represent planarity (*i.e.,* 0˚/360˚ or 180˚).

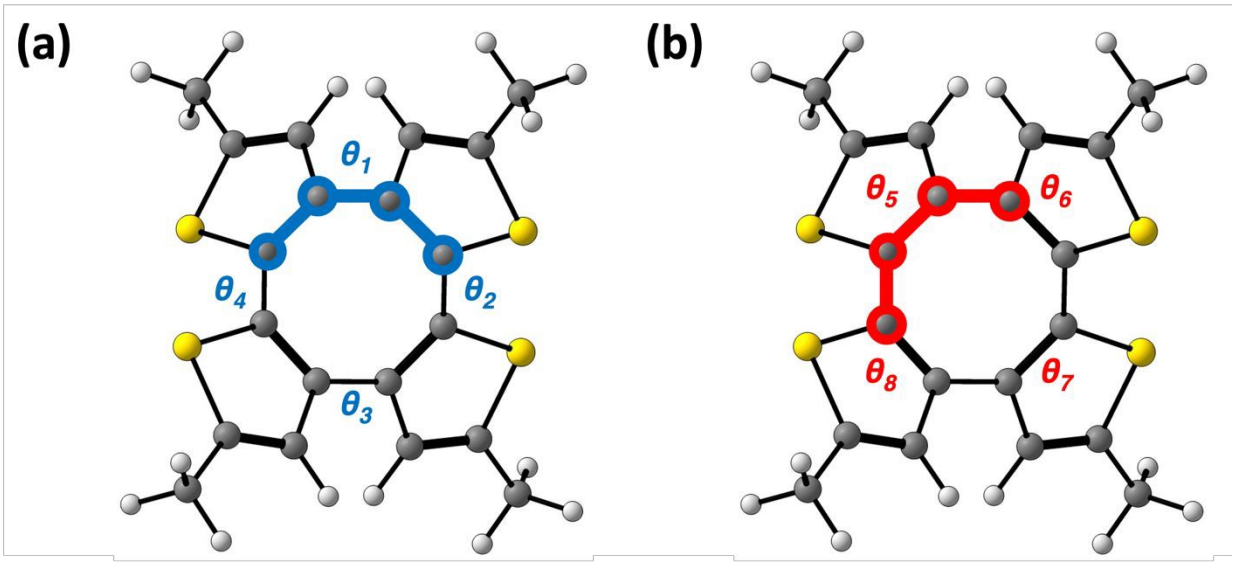


**Figure 7.** The geometrical parameters used to define an absolute planar geometry. We used **(a)** four dihedrals between the thiophenes ($\theta_{1\text{-}4}$) and **(b)** four dihedrals within the thiophenes ($\theta_{5\text{-}8}$) for eight dihedrals. If all the dihedrals are ± 20˚ from planarity (*i.e.,* 0˚/360˚ or 180˚), we classify the geometry as planar.

Based on these geometrical thresholds (*i.e.,* ± 20˚ from 0˚/360˚ and 180˚), we observe that 8% (71) of trajectories access planar geometries. In Figure 8, we investigate a representative trajectory that undergoes the relative inversion mechanism via the planar geometry, as proposed by Ueda *et al.*[25] in more detail.

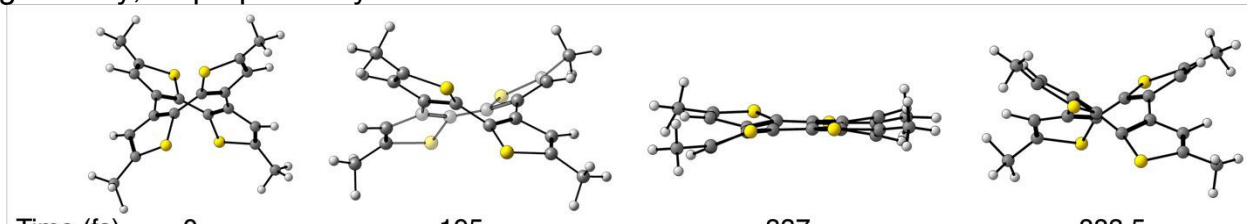

View Article Online
DOI: 10.1039/D6SC00969G



**Figure 8.** A representative trajectory demonstrating the **MeCOTh** to **MeCOTh-b** inversion, driven by the previously hypothesized planar geometry. Snapshots are illustrated at 0 fs, 195 fs, 337 fs, and 883.5 fs during the simulation. The distance between two sulfur atoms from neighboring thiophene rings ($d_{SS}$) and the planarity angle ($\theta_{inv}$) are emphasized below each structure.

We utilized angles $\theta_{1\text{-}8}$ to capture the planar structures systematically; to ensure visual clarity in Figure 8, we emphasize the distance between the two sulfur atoms, $d_{SS}$, and $\theta_{inv}$. At the anticipated planar geometry, $d_{SS}$ is expected to be a minimum, while $\theta_{inv}$ approaches 180˚. At 0 ps, $d_{SS}$ is 3.69 Å and $\theta_{inv}$ is 137˚. By 195 fs, the trajectory has a $d_{SS}$ of 3.24 Å and $\theta_{inv}$ of 157˚. At 337 fs, $d_{SS}$ = 3.08 Å and $\theta_{inv}$ = 175˚. At 883.5 fs, **MeCOTh** shows a $d_{SS}$ of 3.32 Å and $\theta_{inv}$ at 250˚. Between 0 fs and 195 fs, $d_{SS}$ decreased by 0.45 Å, and $\theta_{inv}$ increased by 20˚, indicating a planarizing structure. This dynamical information aligns with the MEP calculation; the **MeCOTh** on the $S_1$-surface planarizes due to Baird aromaticity. Between 196 fs and 337 fs, $d_{SS}$ decreased by 0.16 Å as $\theta_{inv}$ increased by 18˚. This suggests that the planarization observed from 0 fs to 195 fs persists throughout the 196 fs to 337 fs interval; this resulted in a significantly planar structure at 337 fs. Between 338 fs and 883.5 fs, $d_{SS}$ increased by 0.24 Å while $\theta_{inv}$ rose by 75˚. This suggests that inversion occurs after the trajectory assumes a planar conformation, as $d_{SS}$ rises concurrently with $\theta_{inv}$ approaching the torsional region that indicates the relative stereochemistry of **MeCOTh-b**. At the 883.5 fs geometry, the boat-boat conformation facilitates the $S_1 \rightarrow S_0$ surface hopping event.[71] We conclude that these trajectories undergo a direct inversion, passing through a planar structure resulting from the Baird aromatic COT core. We expected to find these results replicated throughout our ML-accelerated NAMD simulations. However, our ML-NAMD trajectories indicate that other pathways outcompete it.

We identified a reaction pathway that involves a new geometry we labeled "crown," characterized by the unidirectional orientation of all sulfur atoms (Figure 9a). We used the defined structural parameters, including $\theta_{inv}$, $\theta_{1\text{-}8}$, and $d_{SS}$, to identify the crown-like geometries from the trajectories automatically. We illustrate the geometrical parameters in Figure 9b-d.

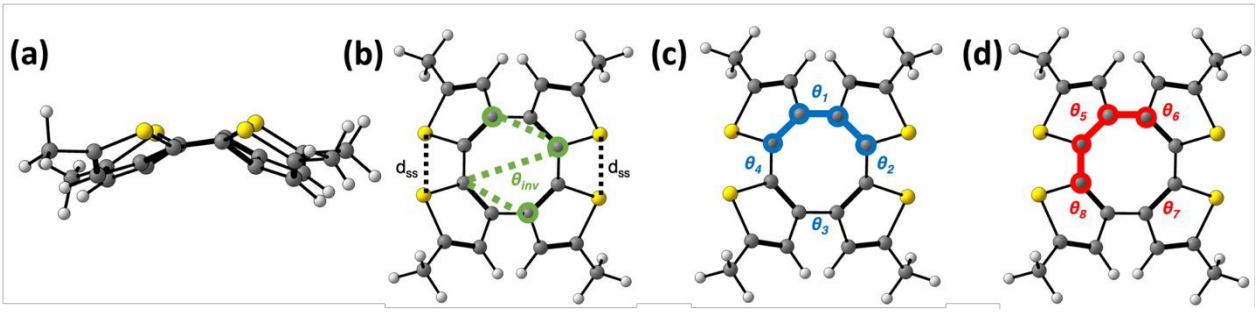


**Figure 9.** Geometrical parameters that define the (a) crown conformation. To systematically capture this geometry in our ML-NAMD trajectories, we tracked the following: (b) the inversion angle ($\theta_{inv}$), sulfur-sulfur distance ($d_{SS}$), (c) four dihedral angles between the thiophenes ($\theta_{1\text{-}4}$), and (d) four dihedral angles within the thiophenes ($\theta_{5\text{-}8}$). A structure is classified as adopting the crown geometry when the following thresholds are met: $\theta_{inv}$ must deviate from planarity (outside ± 20° from 180°), $\theta_{1\text{-}4}$ should be near-

View Article Online
DOI: 10.1039/D6SC00969G



planarity (within ±20° of 0°, 180°, or 360°), $\theta_{5\text{-}8}$ should deviate from planarity (outside ±20° of 0°, 180°, or 360°), and at least one sulfur-sulfur distance must be less than 3.0 Å.

62% (588) of trajectories undergo the **MeCOTh** → **MeCOTh-b** inversion through a crown geometry. In Figure 10, we investigate a representative trajectory that underwent the relative stereochemical inversion via the crown geometry in more detail.

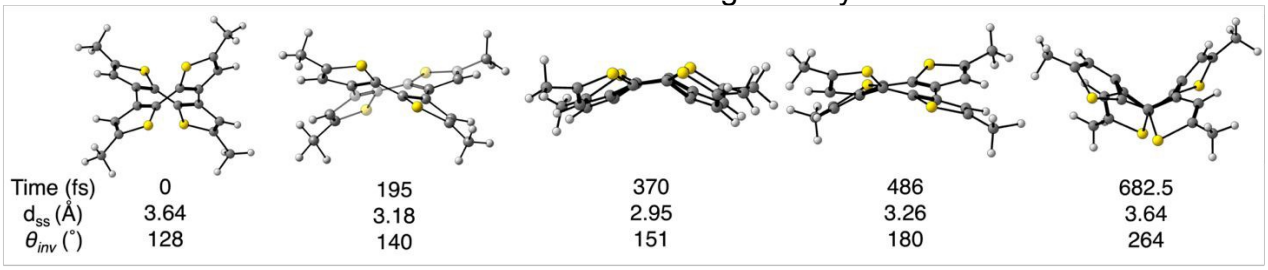


**Figure 10.** A representative trajectory demonstrating the **MeCOTh** to **MeCOTh-b** inversion, driven by the newly proposed crown geometry (t = 370 fs). Key geometries are illustrated at 0 fs, 195 fs, 370 fs, 486 fs, and 682.5 fs during the simulation. $d_{SS}$ and $\theta_{inv}$ are emphasized below each structure.

We report the distance $d_{SS}$ and $\theta_{inv}$ to ensure a direct comparison with Figure 8. At 0 ps, $d_{SS}$ is 3.64 Å, and $\theta_{inv}$ is 128˚. By 195 fs, the trajectory has a $d_{SS}$ of 3.18 Å and $\theta_{inv}$ of 140˚. At 370 fs, $d_{SS}$ measures 2.95 Å, while $\theta_{inv}$ is 151˚. By 486 fs, $d_{SS}$ is 3.26 Å, and $\theta_{inv}$ is 180˚. Finally, at 682.5 fs, $d_{SS}$ is 3.64 Å and $\theta_{inv}$ is 264˚, respectively. Between 0 fs and 195 fs, $d_{SS}$ decreased by 0.46 Å while $\theta_{inv}$ increased by 12˚, indicating an increasingly planar structure within the first 200 fs of the simulation. These structural changes resemble those seen in the trajectory that inverts via the planar geometry (Figure 10), demonstrating **MeCOTh** planarizing on the $S_1$-surface because of Baird aromaticity. From 196 fs to 370 fs, $d_{SS}$ decreased by 0.23 Å, and $\theta_{inv}$ increased by 11˚. The persistent decline in $d_{SS}$ and increase in $\theta_{inv}$ indicate further planarity; however, by 370 fs, **MeCOTh** adopted a crown geometry. We attribute the crown geometry to a balance between the closed-shell repulsions between neighboring sulfurs and the stabilizing effects of Baird aromaticity. $d_{SS}$ rises by 0.31 Å, while $\theta_{inv}$ increases by 29˚, from 371 fs to 486 fs. Indeed, increased $d_{SS}$ indicates that inversion occurs after the crown structure as the sulfur atoms (*i.e.,* thiophene rings) separate. Within this interval, $\theta_{inv}$ increased to 180˚, suggesting a planar structure, similar to the $S_1$ minimum energy structure reported by Ueda *et al.*[25]. However, the non-planar characteristics of the 486-fs geometry imply that trajectories can invert their relative stereochemistries (*i.e.,* pass $\theta_{inv}$ = 180˚) without planarizing. Between 487 fs and 682.5 fs, $d_{SS}$ increased by 0.38 Å and $\theta_{inv}$ by 84˚, illustrating the completion of the relative stereochemical inversion of **MeCOTh** to **MeCOTh-b**. By 682.5 fs, **MeCOTh** exhibits a boat-boat conformation that facilitates the $S_1 \rightarrow S_0$ surface hopping event.[71] We conclude that the mechanism illustrated in Figure 9 is the preferred mechanistic pathway for the **MeCOTh** → **MeCOTh-b** inversion (62% of the trajectories).

## Conclusion

This study provides a complete enumeration of the mechanistic pathways for the relative stereochemical inversion of **MeCOTh** to **MeCOTh-b**, while also assessing the role of Baird aromaticity in the mechanism. We employed multiconfigurational quantum

View Article Online
DOI: 10.1039/D6SC00969G



mechanical computations, combined with ML-NAMD, to provide mechanistic insights into this relative stereochemical inversion in static and dynamic perspectives. We addressed the computational challenges associated with the SA5-CASSCF(8,7)/ANO-S-VDZP NAMD simulations by training multilayer perceptron NNs using our open-source software, PyRAI$^2$MD, which enabled us to accelerate the photodynamic simulations by five orders of magnitude. We utilized our trained NNs to conduct ML-NAMD simulations and outlined the excited-state mechanistic pathways of **MeCOTh → MeCOTh-b**.

Our static, minimum energy path calculation led to a more planar structure (**MeCOTh-MEP-11**) relative to the optimized $S_0$-state geometry (**MeCOTh-$S_0$**); albeit, both had a tub conformation. We optimized **MeCOTh-MEP-11** to an $S_1$-minimum with a boat-boat conformation (**MeCOTh-$S_1$**) featuring a small $S_1/S_0$ gap (0.30 eV). Our static calculation results show that the steepest-descent path on $S_1$ leads to a nonradiative decay channel, but it does not involve the relative stereochemical inversion. The discrepancy between experimental and computational results suggests that our static calculations lack essential dynamical effects. Our ML-NAMD simulations provide critical mechanistic insights and predict quantum yields of 68% for **MeCOTh-b** and 32% for **MeCOTh**. The ML-NAMD calculations demonstrate that 74% of trajectories undergo relative stereochemical inversion entirely on the $S_1$ surface, consistent with the lower $S_1$-state inversion barrier of 4.3 kcal mol$^{-1}$. In contrast, only 25% of trajectories undergo relative stereochemical inversions on the ground state, aligning with the higher $S_0$-state inversion barrier of 25.4 kcal mol$^{-1}$. All productive trajectories exhibit planarizing COT cores, consistent with MEP findings and previous studies that emphasize the role of Baird aromaticity in this reaction mechanism. We identified two competing pathways for inversion, influenced by differing electronic effects: Baird aromaticity and S-S closed-shell repulsions. In 62% of the trajectories, the inversion mechanism is mainly influenced by the balance between S-S closed-shell repulsions and Baird aromaticity, which directs the pathway towards relative stereochemical inversion via a crown geometry characterized by unidirectional sulfurs. Conversely, in 8% of the trajectories, Baird aromaticity overcomes S-S closed-shell repulsions, steering the trajectory towards relative stereochemical inversion through a planar geometry. Thus, the dominant inversion pathway passes through the newly labeled crown geometry on the $S_1$ surface rather than the previously proposed planar geometry. Thus, the dominant inversion pathway passes through the newly labeled crown geometry on the $S_1$ surface rather than the previously proposed planar geometry.

While previous studies have focused on the aromaticity reversal and subsequent planarization of the COT-core of **MeCOTh** and other COT-derivatives as the main drivers of their aggregate-induced emission[48], polymerization control[90], and thermosalient effect[91], our findings suggest a competing driver for these macroscopic effects: the balance between S-S closed-shell repulsions and Baird aromaticity. This competing mechanistic pathway illustrates a potential competing driver for these macroscopic effects that may impede intramolecular motions[48], disrupt hydrogen bonding networks[90, 91], and interfere with beneficial π-stacking[91], within these COT-based materials.

One of the main findings in the 2017 report by Ueda *et al.* was the temperature-dependent racemization of **MeCOTh**. Although exploring the temperature dependence of the reaction mechanism presented here is beyond the scope of this manuscript, we argue that our reported mechanism is temperature dependent. We hypothesize that an increase

View Article Online
DOI: 10.1039/D6SC00969G



in temperature would provide sufficient thermal energy to facilitate the adoption of **MeCOTh-crown**, thus facilitating racemization. This remains to be explored in future studies.

## Computational Methods

### Multiconfigurational methods

We performed multiconfigurational calculations using a state-averaged complete active space self-consistent field (SA-CASSCF) method in OpenMolcas 19.11.[92] This approach utilizes the format SA(N)-CASSCF(m,n), where N signifies the number of singlet states averaged in the calculation. The variables m and n denote the number of electrons and orbitals in the active space. To be conscientious of the computational cost associated with CASSCF methodology, we aimed to construct the smallest possible active space that captured the photophysical properties of **MeCOTh**. To this end, we selected an active space consisting of eight electrons within seven orbitals (*i.e.,* 4 π-orbital and 3 π*-orbital; Figure 1). We optimized minima on the $S_0$ and $S_1$ surfaces, performed vibrational analysis to verify the stationary points, predicted the absorption spectra, and computed a minimum-energy path using SA5-CASSCF(8,7) with the ANO-S-VDZP basis set. We employed complete active space second-order perturbation theory to account for dynamic correlations in the minimum-energy path calculation. We applied multistate complete active space second-order perturbation theory to predict absorption spectra. To demonstrate the need for machine learning to study the inversion mechanism of **MeCOTh**, we benchmarked a single-step quantum-mechanical nonadiabatic molecular dynamics simulation of **MeCOTh** using SA5-CASSCF(8,7)/ANO-S-VDZP, which took 3.23 hours. Performing a single 1-picosecond QM-NAMD simulation, involving a series of 2,000 single-point and gradient calculations, would take approximately 269 days.

### Singe-reference method

We used density functional theory (DFT) to optimize the ground-state global minima of **MeCOTh** using the CAM-B3LYP-GD3(BJ)/6-31G(d,p). We used time-dependent density functional theory (TD-DFT) to calculate the excitation energies for the first 10 excited states of **MeCOTh**. The TD-DFT calculations were run using the CAM-B3LYP-GD3(BJ) and ωB97X-D functionals with the aug-cc-pVDZ basis set. All DFT calculations were performed using Gaussian 16.[75]

### Training data generation and NN training

We generated the initial training dataset in two sections: Wigner sampling and geometric interpolation. We performed Wigner sampling based on the frequencies of the ground-state, SA5-CASSCF(8,7)/ANO-S-VDZP optimized geometry of **MeCOTh** to generate 160 structures at the zero-point energy level. The geometric interpolation produced 8 structures, spanning from the Franck-Condon point of **MeCOTh** to an $S_1/S_0$ minimum energy conical intersection (MECI), and an additional 8 structures from the $S_1/S_0$ MECI to the inverted relative stereochemical product, **MeCOTh-b**; totaling 16 intermediate structures. We utilized the nuclear displacements from the 160 Wigner-sampled structures to adjust the interpolated geometries, resulting in 2560 initial data points. A SA5-CASSCF(8,7)/ANO-S-VDZP single-point calculation was performed on all data points to obtain their respective $S_0$ and $S_1$ energies and gradients. This data set was used to train our initial neural network (NN) potentials.

View Article Online
DOI: 10.1039/D6SC00969G



We employ the TensorFlow/Keras API in Python to construct and train the NN potential.[93] We constructed a fully connected feedforward multilayer perceptron NN that utilizes leaky softplus activation functions. The NN calculates the inverse distance of the input molecule to predict energies and forces. We simultaneously train the NN using energy and forces to maintain their physical relationship. The learning rate is set to $10^{-3}$ and incorporates a scheduler that reduces it to $10^{-4}$ and $10^{-5}$ when the validation loss plateaus. The dataset is split into training and validation sets with a 9:1 ratio. Additional information can be found in the Supporting Information.

To expand the initial training set with undersampled data, we used a committee model of two NNs (Table S2) to propagate 150 trajectories from the $S_1$ state for 10 ps with a step size of 0.5 fs. The standard deviation in the predicted energy and gradients by the NN committee served as a measure of uncertainty for the current prediction. The trajectories were halted when the standard deviation surpassed the energy and gradient thresholds. Based on our experience, we established the thresholds for energy and gradient at 0.04 Hartree and 0.25 Hartree·Bohr$^{-1}$, respectively, to effectively detect uncertain structures and enhance the NN potential. The final geometries of the halted trajectories were recalculated using SA5-CASSCF(8,7)/ANO-S-VDZP and added to the initial training set. Subsequently, adaptive sampling retrained the committee model using the updated dataset and restarted the trajectories. The process was repeated iteratively until no new structures emerged; this led to 52 iterations and a data set with 4207 total data points. The mean absolute errors in the predicted energies were 0.045 eVs and 0.046 eVs.

**ML-photodynamics simulations**

We used the NNs from the latest iteration of adaptive sampling (iteration 52) to propagate 988 ML-NAMD trajectories for 5.5 ps with a 0.5 fs time step. The probabilities of nonadiabatic electronic transitions were computed with Tully's FSSH method[87], where we used the curvature-driven time derivative coupling (*k*TDC) to evaluate the nonadiabatic couplings based on the energy gaps predicted by the NNs. [88, 89] The *k*TDC method showed accuracy when compared to ground-truth NAC values derived from quantum mechanical calculations.[88, 89] It was especially effective for small energy gaps (*e.g.,* <0.5 eV).[88]

**Conflicts of interest**

There are no conflicts of interest to declare.

**Acknowledgements**

This work was supported by the National Science Foundation Center under NSF-CHE-2144556. All authors appreciate the assistance from the Northeastern Research Computing Team and the computing resources provided by the Massachusetts Life Science Center grant (G00006360).

References

(1) Cho, S.; Usuba, J.; Chakraborty, S.; Li, X.; Han, G. G. D. Solid-state photon energy storage via reversible [2+2] cycloaddition of donor-acceptor styrylpyrylium system. *Chem* **2023**. DOI: 10.1016/j.chempr.2023.06.007.

(2) Poloukhtine, A. A.; Mbua, N. E.; Wolfert, M. A.; Boons, G.-J.; Popik, V. V. Selective Labeling of Living Cells by a Photo-Triggered Click Reaction. *Journal of the American Chemical Society* **2009**, *131* (43), 15769-15776. DOI: 10.1021/ja9054096.

View Article Online
DOI: 10.1039/D6SC00969G



(3) Li, G.; Li, Q.-S.; Xie, Y.; King, R. B.; Schaefer, H. F. (Acetylene)dicobalt Carbonyl Derivatives: Decarbonylation of the H 2 C 2 Co 2 (CO) 6 Tetrahedrane. *Organometallics.* **2009**, *28* (12), 3390-3394. DOI: 10.1021/om801211g.
(4) Chang, M. H.; Dougherty, D. A. Photochemistry of 2,3-diazabicyclo[2.1.1]hex-2-ene. .beta. Carbon-carbon cleavage to a stereorandom triplet biradical. *Journal of the American Chemical Society* **1982**, *104* (8), 2333-2334. DOI: 10.1021/ja00372a050.
(5) Zhu, S.; Jia, L.; Cheng, Q.; Sun, Q.; Chen, X.; Yu, H.; Han, Y.; Hou, H. Visible-Light-Induced Stereoselective Radical trans-Iodoalkylation of Terminal Alkyne with Iodoform. *Org Lett* **2024**, *26* (39), 8400-8404. DOI: 10.1021/acs.orglett.4c03241.
(6) Noble, A.; McCarver, S. J.; MacMillan, D. W. Merging photoredox and nickel catalysis: decarboxylative cross-coupling of carboxylic acids with vinyl halides. *J Am Chem Soc* **2015**, *137* (2), 624-627. DOI: 10.1021/ja511913h.
(7) Andrews, S. D.; Day, A. C. The photolysis of 4-alkylidene-Δ1-pyrazolines: a route to trimethylenemethyls. *Chemical Communications (London)* **1966**, (19), 667-669, 10.1039/C19660000667. DOI: 10.1039/C19660000667.
(8) Kar, S.; Sanderson, H.; Roy, K.; Benfenati, E.; Leszczynski, J. Green Chemistry in the Synthesis of Pharmaceuticals. *Chem Rev* **2022**, *122* (3), 3637-3710. DOI: 10.1021/acs.chemrev.1c00631.
(9) Long, T.; Pan, S.; Zhu, S.; Chu, L. Catalyst-Free Intermolecular Sulfonyl/Fluoromethyl Heteroarylation of Vinyl Ethers via Visible-Light-Induced Charge Transfer. *Chemistry* **2022**, *28* (15), e202104080. DOI: 10.1002/chem.202104080.
(10) Dorman, G.; Prestwich, G. D. Benzophenone Photophores in Biochemistry. *Biochemistry* **1994**, *33* (19), 5661-5673. DOI: 10.1021/bi00185a001.
(11) Smith, E.; Collins, I. Photoaffinity labeling in target- and binding-site identification. *Future Med Chem* **2015**, *7* (2), 159-183. DOI: 10.4155/fmc.14.152.
(12) Kumar, A. B.; Tipton, J. D.; Manetsch, R. 3-Trifluoromethyl-3-aryldiazirine photolabels with enhanced ambient light stability. *Chem Commun (Camb)* **2016**, *52* (13), 2729-2732. DOI: 10.1039/c5cc09518b.
(13) Al-Kaysi, R. O.; Tong, F.; Al-Haidar, M.; Zhu, L.; Bardeen, C. J. Highly branched photomechanical crystals. *Chem Commun (Camb)* **2017**, *53* (17), 2622-2625. DOI: 10.1039/c6cc08999b.
(14) Koshima, H.; Ojima, N.; Uchimoto, H. Mechanical Motion of Azobenzene Crystals upon Photoirradiation. *Journal of the American Chemical Society* **2009**, *131* (20), 6890-6891. DOI: 10.1021/ja8098596.
(15) Lennartson, A.; Roffey, A.; Moth-Poulsen, K. Designing photoswitches for molecular solar thermal energy storage. *Tetrahedron Letters* **2015**, *56* (12), 1457-1465. DOI: 10.1016/j.tetlet.2015.01.187.
(16) Beharry, A. A.; Wong, L.; Tropepe, V.; Woolley, G. A. Fluorescence imaging of azobenzene photoswitching in vivo. *Angew Chem Int Ed Engl* **2011**, *50* (6), 1325-1327. DOI: 10.1002/anie.201006506.
(17) Yoneda, Y.; Konishi, T.; Suga, K.; Saito, S.; Kuramochi, H. Excited-State Aromatization Drives Nonequilibrium Planarization Dynamics. *J Am Chem Soc* **2025**, *147* (14), 12051-12060. DOI: 10.1021/jacs.4c18623.
(18) Lee, H.; Tessarolo, J.; Langbehn, D.; Baksi, A.; Herges, R.; Clever, G. H. Light-Powered Dissipative Assembly of Diazocine Coordination Cages. *Journal of the American Chemical Society* **2022**, *144* (7), 3099-3105. DOI: 10.1021/jacs.1c12011.

View Article Online
DOI: 10.1039/D6SC00969G



(19) Shields, D. J.; Karothu, D. P.; Sambath, K.; Ranaweera, R.; Schramm, S.; Duncan, A.; Duncan, B.; Krause, J. A.; Gudmundsdottir, A. D.; Naumov, P. Cracking under Internal Pressure: Photodynamic Behavior of Vinyl Azide Crystals through N(2) Release. *J Am Chem Soc* **2020**, *142* (43), 18565-18575. DOI: 10.1021/jacs.0c07830.
(20) Yamamoto, N.; Olivucci, M.; Celani, P.; Bernardi, F.; Robb, M. A. An MC-SCF/MP2 Study of the Photochemistry of 2,3-Diazabicyclo[2.2.1]hept-2-ene: Production and Fate of Diazenyl and Hydrazonyl Biradicals. *Journal of the American Chemical Society* **1998**, *120* (10), 2391-2407. DOI: 10.1021/ja971733v.
(21) Huang, Y.; Zheng, X.; Wu, J.; Gao, Y.; Ling, Q.; Lin, Z. Photoinduced pi-Bond breakage causing dynamic closing-opening shell transition of Z-type Diphenylmaleonitriles molecules. *Nat Commun* **2024**, *15* (1), 6514. DOI: 10.1038/s41467-024-50943-4.
(22) Kobatake, S.; Kitagawa, D. Photoresponsive Molecular Crystals for Light-Driven Photoactuators. In *Photosynergetic Responses in Molecules and Molecular Aggregates*, Miyasaka, H., Matsuda, K., Abe, J., Kawai, T. Eds.; Springer Singapore, 2020; pp 427-447.
(23) Skolia, E.; Kokotos, C. G. Photochemical [2 + 2] Cycloaddition of Alkenes with Maleimides: Highlighting the Differences between N-Alkyl vs N-Aryl Maleimides. *ACS Org Inorg Au* **2023**, *3* (2), 96-103. DOI: 10.1021/acsorginorgau.2c00053.
(24) Yan, J.; Slanina, T.; Bergman, J.; Ottosson, H. Photochemistry Driven by Excited-State Aromaticity Gain or Antiaromaticity Relief. *Chemistry* **2023**, *29* (19), e202203748. DOI: 10.1002/chem.202203748.
(25) Ueda, M.; Jorner, K.; Sung, Y. M.; Mori, T.; Xiao, Q.; Kim, D.; Ottosson, H.; Aida, T.; Itoh, Y. Energetics of Baird aromaticity supported by inversion of photoexcited chiral [4n]annulene derivatives. *Nature Communications* **2017**, *8* (1), 346. DOI: 10.1038/s41467-017-00382-1.
(26) Drazenovic, J.; Laconsay, C. J.; Doslic, N.; J, I. C. W.; Basaric, N. Excited-state antiaromaticity relief drives facile photoprotonation of carbons in aminobiphenyls. *Chem Sci* **2024**, *15* (14), 5225-5237. DOI: 10.1039/d4sc00642a.
(27) Li, X.; Cho, S.; Wan, J.; Han, G. G. D. Photoswitches and photochemical reactions for optically controlled phase transition and energy storage. *Chem* **2023**, *9* (9), 2378-2389. DOI: 10.1016/j.chempr.2023.05.029.
(28) Manso, M.; Petersen, A. U.; Wang, Z.; Erhart, P.; Nielsen, M. B.; Moth-Poulsen, K. Molecular solar thermal energy storage in photoswitch oligomers increases energy densities and storage times. *Nat Commun* **2018**, *9* (1), 1945. DOI: 10.1038/s41467-018-04230-8.
(29) López-Cano, M.; Scortichini, M.; Tosh, D. K.; Salmaso, V.; Ko, T.; Salort, G.; Filgaira, I.; Soler, C.; Trauner, D.; Hernando, J.; et al. Photoswitchable Diazocine Derivative for Adenosine A3 Receptor Activation in Psoriasis. *Journal of the American Chemical Society* **2025**, *147* (1), 874-879. DOI: 10.1021/jacs.4c13558.
(30) Wang, B. Y.; Lin, Y. C.; Lai, Y. T.; Ou, J. Y.; Chang, W. W.; Chu, C. C. Targeted photoresponsive carbazole-coumarin and drug conjugates for efficient combination therapy in leukemia cancer cells. *Bioorg Chem* **2020**, *100*, 103904. DOI: 10.1016/j.bioorg.2020.103904.

View Article Online
DOI: 10.1039/D6SC00969G



(31) Shaw, P. A.; Klausen, M.; Bradley, M. A dual action coumarin-camptothecin polymer for light responsive drug release and photodynamic therapy. *Polym Chem* **2024**, *15* (2), 54-58. DOI: 10.1039/d3py01137b.
(32) Rosenberg, M.; Dahlstrand, C.; Kilså, K.; Ottosson, H. Excited State Aromaticity and Antiaromaticity: Opportunities for Photophysical and Photochemical Rationalizations. *Chemical Reviews* **2014**, *114* (10), 5379-5425. DOI: 10.1021/cr300471v.
(33) Merino, G.; Sola, M.; Fernandez, I.; Foroutan-Nejad, C.; Lazzeretti, P.; Frenking, G.; Anderson, H. L.; Sundholm, D.; Cossio, F. P.; Petrukhina, M. A.; et al. Aromaticity: Quo Vadis. *Chem Sci* **2023**, *14* (21), 5569-5576. DOI: 10.1039/d2sc04998h.
(34) Ottosson, H. A focus on aromaticity: fuzzier than ever before? *Chem Sci* **2023**, *14* (21), 5542-5544. DOI: 10.1039/d3sc90075d.
(35) Schleyer, P. v. R. Introduction: Aromaticity. *Chemical Reviews* **2001**, *101* (5), 1115-1118. DOI: 10.1021/cr0103221.
(36) XX. On new compounds of carbon and hydrogen, and on certain other products obtained during the decomposition of oil by heat. *Philosophical transactions of the Royal Society of London.* **1825**, *115*, 440-466. DOI: 10.1098/rstl.1825.0022.
(37) Hückel, E. Quantentheoretische Beiträge zum Benzolproblem. *Zeitschrift fur Physik* **1931**, *70*, 204-286. DOI: 10.1007/BF01339530.
(38) Aromatic Character. *Chemical & Engineering News Archive* **1965**, *43* (26), 90-100. DOI: 10.1021/cen-v043n026.p090.
(39) Dewar, M. J. S. A molecular orbital theory of organic chemistry—VIII: romaticity and electrocyclic reactions. *Tetrahedron* **1966**, *22*, 75-92. DOI: https://doi.org/10.1016/S0040-4020(01)82171-2.
(40) Baird, N. C. Quantum organic photochemistry. II. Resonance and aromaticity in the lowest 3.pi..pi.* state of cyclic hydrocarbons. *Journal of the American Chemical Society* **1972**, *94* (14), 4941-4948. DOI: 10.1021/ja00769a025.
(41) Karadakov, P. B. Ground- and Excited-State Aromaticity and Antiaromaticity in Benzene and Cyclobutadiene. *The Journal of Physical Chemistry A* **2008**, *112* (31), 7303-7309. DOI: 10.1021/jp8037335.
(42) Karadakov, P. B. Aromaticity and Antiaromaticity in the Low-Lying Electronic States of Cyclooctatetraene. *The Journal of Physical Chemistry A* **2008**, *112* (49), 12707-12713. DOI: 10.1021/jp8067365.
(43) Oh, J.; Sung, Y. M.; Mori, H.; Park, S.; Jorner, K.; Ottosson, H.; Lim, M.; Osuka, A.; Kim, D. Unraveling Excited-Singlet-State Aromaticity via Vibrational Analysis. *Chem* **2017**, *3* (5), 870-880. DOI: 10.1016/j.chempr.2017.09.005.
(44) Sung, Y. M.; Oh, J.; Naoda, K.; Lee, T.; Kim, W.; Lim, M.; Osuka, A.; Kim, D. A Description of Vibrational Modes in Hexaphyrins: Understanding the Aromaticity Reversal in the Lowest Triplet State. *Angew Chem Int Ed Engl* **2016**, *55* (39), 11930-11934. DOI: 10.1002/anie.201603631.
(45) Karas, L. J.; Wu, C. H.; Wu, J. I. Barrier-Lowering Effects of Baird Antiaromaticity in Photoinduced Proton-Coupled Electron Transfer (PCET) Reactions. *J Am Chem Soc* **2021**, *143* (43), 17970-17974. DOI: 10.1021/jacs.1c09324.
(46) Kim, J.; Oh, J.; Park, S.; Zafra, J. L.; DeFrancisco, J. R.; Casanova, D.; Lim, M.; Tovar, J. D.; Casado, J.; Kim, D. Two-electron transfer stabilized by excited-state aromatization. *Nat Commun* **2019**, *10* (1), 4983. DOI: 10.1038/s41467-019-12986-w.

View Article Online
DOI: 10.1039/D6SC00969G



(47) Lampkin, B. J.; Nguyen, Y. H.; Karadakov, P. B.; VanVeller, B. Demonstration of Baird's rule complementarity in the singlet state with implications for excited-state intramolecular proton transfer. *Phys Chem Chem Phys* **2019**, *21* (22), 11608-11614. DOI: 10.1039/c9cp02050k.
(48) Zhao, Z.; Zheng, X.; Du, L.; Xiong, Y.; He, W.; Gao, X.; Li, C.; Liu, Y.; Xu, B.; Zhang, J.; et al. Non-aromatic annulene-based aggregation-induced emission system via aromaticity reversal process. *Nat Commun* **2019**, *10* (1), 2952. DOI: 10.1038/s41467-019-10818-5.
(49) Saito, S.; Nobusue, S.; Tsuzaka, E.; Yuan, C.; Mori, C.; Hara, M.; Seki, T.; Camacho, C.; Irle, S.; Yamaguchi, S. Light-melt adhesive based on dynamic carbon frameworks in a columnar liquid-crystal phase. *Nat Commun* **2016**, *7*, 12094. DOI: 10.1038/ncomms12094.
(50) Kalapos, P. P.; Mayer, P. J.; Gazdag, T.; Demeter, A.; Oruganti, B.; Durbeej, B.; London, G. Photoswitching of Local (Anti)Aromaticity in Biphenylene-Based Diarylethene Molecular Switches. *J Org Chem* **2022**, *87* (15), 9532-9542. DOI: 10.1021/acs.joc.2c00504.
(51) Paul, S.; Kitakado, H.; Suga, K.; Kotani, R.; Dey, N.; Venkatramani, R.; Matito, E.; Saito, S.; Dasgupta, J. Triplet conformation in chromophore-fused cyclooctatetraene dyes. *Journal of Materials Chemistry C* **2023**. DOI: 10.1039/d3tc02151c.
(52) Pati, A. K.; El Bakouri, O.; Jockusch, S.; Zhou, Z.; Altman, R. B.; Fitzgerald, G. A.; Asher, W. B.; Terry, D. S.; Borgia, A.; Holsey, M. D.; et al. Tuning the Baird aromatic triplet-state energy of cyclooctatetraene to maximize the self-healing mechanism in organic fluorophores. *Proc Natl Acad Sci U S A* **2020**, *117* (39), 24305-24315. DOI: 10.1073/pnas.2006517117.
(53) Slanina, T.; Ayub, R.; Toldo, J.; Sundell, J.; Rabten, W.; Nicaso, M.; Alabugin, I.; Fdez Galvan, I.; Gupta, A. K.; Lindh, R.; et al. Impact of Excited-State Antiaromaticity Relief in a Fundamental Benzene Photoreaction Leading to Substituted Bicyclo[3.1.0]hexenes. *J Am Chem Soc* **2020**, *142* (25), 10942-10954. DOI: 10.1021/jacs.9b13769.
(54) Mohamed, R. K.; Mondal, S.; Jorner, K.; Delgado, T. F.; Lobodin, V. V.; Ottosson, H.; Alabugin, I. V. The Missing C1-C5 Cycloaromatization Reaction: Triplet State Antiaromaticity Relief and Self-Terminating Photorelease of Formaldehyde for Synthesis of Fulvenes from Enynes. *J Am Chem Soc* **2015**, *137* (49), 15441-15450. DOI: 10.1021/jacs.5b07448.
(55) Papadakis, R.; Ottosson, H. The excited state antiaromatic benzene ring: a molecular Mr Hyde? *Chem Soc Rev* **2015**, *44* (18), 6472-6493. DOI: 10.1039/c5cs00057b.
(56) Wan, P.; Krogh, E. Evidence for the generation of aromatic cationic systems in the excited state. Photochemical solvolysis of fluoren-9-ol. *Journal of the Chemical Society, Chemical Communications* **1985**, (17), 1207-1208, 10.1039/C39850001207. DOI: 10.1039/C39850001207.
(57) Kotani, R.; Sotome, H.; Okajima, H.; Yokoyama, S.; Nakaike, Y.; Kashiwagi, A.; Mori, C.; Nakada, Y.; Yamaguchi, S.; Osuka, A.; et al. Flapping viscosity probe that shows polarity-independent ratiometric fluorescence. *Journal of Materials Chemistry C* **2017**, *5* (21), 5248-5256. DOI: 10.1039/c7tc01533j.
(58) Yamakado, T.; Takahashi, S.; Watanabe, K.; Matsumoto, Y.; Osuka, A.; Saito, S. Conformational Planarization versus Singlet Fission: Distinct Excited-State Dynamics of

View Article Online
DOI: 10.1039/D6SC00969G

Cyclooctatetraene-Fused Acene Dimers. *Angew Chem Int Ed Engl* **2018**, *57* (19), 5438-5443. DOI: 10.1002/anie.201802185.
(59) Xing, D.; Glocklhofer, F.; Plasser, F. Proton transfer induced excited-state aromaticity gain for chromophores with maximal Stokes shifts. *Chem Sci* **2024**, *15* (43), 17918-17926. DOI: 10.1039/d4sc04692g.
(60) Shukla, D.; Wan, P. Evidence for a planar cyclically conjugated 8.pi. system in the excited state: large Stokes shift observed for dibenz[b,f]oxepin fluorescence. *Journal of the American Chemical Society* **1993**, *115* (7), 2990-2991. DOI: 10.1021/ja00060a063.
(61) Klärner, F.-G. About the Antiaromaticity of Planar Cyclooctatetraene. *Angewandte Chemie International Edition* **2001**, *40* (21), 3977-3981. DOI: https://doi.org/10.1002/1521-3773(20011105)40:21<3977::AID-ANIE3977>3.0.CO;2-N (acccessed 2025/05/02).
(62) Nishinaga, T.; Ohmae, T.; Iyoda, M. Recent Studies on the Aromaticity and Antiaromaticity of Planar Cyclooctatetraene. *Symmetry* **2010**, *2* (1), 76-97. DOI: 10.3390/sym2010076.
(63) Wu, J. I.; Fernandez, I.; Mo, Y.; Schleyer, P. Why Cyclooctatetraene Is Highly Stabilized: The Importance of "Two-Way" (Double) Hyperconjugation. *J Chem Theory Comput* **2012**, *8* (4), 1280-1287. DOI: 10.1021/ct3000553.
(64) Kroeger, A. A.; Karton, A. Graphene-induced planarization of cyclooctatetraene derivatives. *J Comput Chem* **2022**, *43* (2), 96-105. DOI: 10.1002/jcc.26774.
(65) Schild, A.; Paulus, B. Multireference calculations for ring inversion and double bond shifting in cyclooctatetraene. *J Comput Chem* **2013**, *34* (16), 1393-1397. DOI: 10.1002/jcc.23273.
(66) Tokizaki, C.; Yoshida, T.; Takayanagi, T. Quantum transition state dynamics of the cyclooctatetraene unimolecular reaction on ab initio potential energy surfaces. *Chemical Physics* **2016**, *469-470*, 97-104. DOI: 10.1016/j.chemphys.2016.02.005.
(67) Gogonea, V.; Schleyer, P. v. R.; Schreiner, P. R. Consequences of Triplet Aromaticity in 4n π - Electron Annulenes: Calculation of Magnetic Shieldings for Open - Shell Species. *Angewandte Chemie* **1998**, *37*, 1945-1948.
(68) Song, H.; Nam, Y.; Keefer, D.; Garavelli, M.; Mukamel, S.; Tretiak, S. Nonadiabatic Molecular Dynamics Study of the Relaxation Pathways of Photoexcited Cyclooctatetraene. *J Phys Chem Lett* **2021**, *12* (24), 5716-5722. DOI: 10.1021/acs.jpclett.1c01397.
(69) Karadakov, P. B.; Preston, N. Aromaticity reversals and their effect on bonding in the low-lying electronic states of cyclooctatetraene. *Phys Chem Chem Phys* **2021**, *23* (43), 24750-24756. DOI: 10.1039/d1cp04394c.
(70) Feixas, F.; Vandenbussche, J.; Bultinck, P.; Matito, E.; Sola, M. Electron delocalization and aromaticity in low-lying excited states of archetypal organic compounds. *Phys Chem Chem Phys* **2011**, *13* (46), 20690-20703. DOI: 10.1039/c1cp22239b.
(71) Garavelli, M.; Bernardi, F.; Cembran, A.; Castaño, O.; Frutos, L. M.; Merchán, M.; Olivucci, M. Cyclooctatetraene Computational Photo- and Thermal Chemistry: A Reactivity Model for Conjugated Hydrocarbons. *Journal of the American Chemical Society* **2002**, *124* (46), 13770-13789. DOI: 10.1021/ja020741v.
(72) Li, J.; Reiser, P.; Boswell, B. R.; Eberhard, A.; Burns, N. Z.; Friederich, P.; Lopez, S. A. Automatic discovery of photoisomerization mechanisms with nanosecond machine

View Article Online
DOI: 10.1039/D6SC00969G



learning photodynamics simulations. *Chem Sci* **2021**, *12* (14), 5302-5314. DOI: 10.1039/d0sc05610c.
(73) Li, J.; Lopez, S. A. Machine learning accelerated photodynamics simulations. *Chemical Physics Reviews* **2023**, *4* (3), 031309. DOI: 10.1063/5.0159247 (acccessed 9/14/2023).
(74) Li, J.; Stein, R.; Adrion, D. M.; Lopez, S. A. Machine-Learning Photodynamics Simulations Uncover the Role of Substituent Effects on the Photochemical Formation of Cubanes. *J Am Chem Soc* **2021**, *143* (48), 20166-20175. DOI: 10.1021/jacs.1c07725.
(75) Frisch, M. J.; Trucks, G. W.; Schlegel, H. B.; Scuseria, G. E.; Robb, M. A.; Cheeseman, J. R.; Scalmani, G.; Barone, V.; Petersson, G. A.; Nakatsuji, H.; et al. Gaussian 16 Rev. B.01. **2016**.
(76) Yanai, T.; Tew, D. P.; Handy, N. C. A new hybrid exchange–correlation functional using the Coulomb-attenuating method (CAM-B3LYP). *Chemical Physics Letters* **2004**, *393* (1), 51-57. DOI: https://doi.org/10.1016/j.cplett.2004.06.011.
(77) Chai, J.-D.; Head-Gordon, M. Long-range corrected hybrid density functionals with damped atom–atom dispersion corrections. *Physical Chemistry Chemical Physics* **2008**, *10* (44), 6615-6620, 10.1039/B810189B. DOI: 10.1039/B810189B.
(78) Dunning, T. H., Jr. Gaussian basis sets for use in correlated molecular calculations. I. The atoms boron through neon and hydrogen. *The Journal of Chemical Physics* **1989**, *90* (2), 1007-1023. DOI: 10.1063/1.456153 (acccessed 6/6/2025).
(79) Kendall, R. A.; Dunning, T. H., Jr.; Harrison, R. J. Electron affinities of the first - row atoms revisited. Systematic basis sets and wave functions. *The Journal of Chemical Physics* **1992**, *96* (9), 6796-6806. DOI: 10.1063/1.462569 (acccessed 6/6/2025).
(80) Thompson, A. L.; Martinez, T. J. Time-resolved photoelectron spectroscopy from first principles: excited state dynamics of benzene. *Faraday Discuss* **2011**, *150*, 293-311; discussion 391-418. DOI: 10.1039/c1fd00003a.
(81) Li, J.; Lopez, S. A. Multiconfigurational Calculations and Nonadiabatic Molecular Dynamics Explain Tricyclooctadiene Photochemical Chemoselectivity. *J Phys Chem A* **2020**, *124* (38), 7623-7632. DOI: 10.1021/acs.jpca.0c05280.
(82) Finley, J.; Malmqvist, P.-Å.; Roos, B. O.; Serrano-Andrés, L. The multi-state CASPT2 method. *Chemical Physics Letters* **1998**, *288* (2), 299-306. DOI: https://doi.org/10.1016/S0009-2614(98)00252-8.
(83) Boggio-Pasqua, M.; Jacquemin, D.; Loos, P. F. Benchmarking CASPT3 vertical excitation energies. *J Chem Phys* **2022**, *157* (1), 014103. DOI: 10.1063/5.0095887.
(84) Sarkar, R.; Loos, P. F.; Boggio-Pasqua, M.; Jacquemin, D. Assessing the Performances of CASPT2 and NEVPT2 for Vertical Excitation Energies. *J Chem Theory Comput* **2022**, *18* (4), 2418-2436. DOI: 10.1021/acs.jctc.1c01197.
(85) Silva-Junior, M. R.; Schreiber, M.; Sauer, S. P.; Thiel, W. Benchmarks of electronically excited states: basis set effects on CASPT2 results. *J Chem Phys* **2010**, *133* (17), 174318. DOI: 10.1063/1.3499598.
(86) Freitas, M. P. Regio- and stereochemical behavior of cyclooctane and cyclodecane derivatives containing CF2 moieties. *Journal of Fluorine Chemistry* **2025**, *282*. DOI: 10.1016/j.jfluchem.2025.110397.
(87) Tully, J. C. Molecular dynamics with electronic transitions. *The Journal of Chemical Physics* **1990**, *93* (2), 1061-1071. DOI: 10.1063/1.459170.

View Article Online
DOI: 10.1039/D6SC00969G

(88) Zhao, X.; Merritt, I. C. D.; Lei, R.; Shu, Y.; Jacquemin, D.; Zhang, L.; Xu, X.; Vacher, M.; Truhlar, D. G. Nonadiabatic Coupling in Trajectory Surface Hopping: Accurate Time Derivative Couplings by the Curvature-Driven Approximation. *J Chem Theory Comput* **2023**, *19* (19), 6577-6588. DOI: 10.1021/acs.jctc.3c00813.
(89) Shu, Y.; Zhang, L.; Chen, X.; Sun, S.; Huang, Y.; Truhlar, D. G. Nonadiabatic Dynamics Algorithms with Only Potential Energies and Gradients: Curvature-Driven Coherent Switching with Decay of Mixing and Curvature-Driven Trajectory Surface Hopping. *J Chem Theory Comput* **2022**, *18* (3), 1320-1328. DOI: 10.1021/acs.jctc.1c01080.
(90) Aoki, T.; Ueda, M.; Aida, T.; Itoh, Y. Supramolecular Polymerization of a Photo-Fluttering Chiral Monomer: A Temporarily Suspendable Chain Growth by Light. *J Am Chem Soc* **2022**, *144* (16), 7080-7084. DOI: 10.1021/jacs.2c02176.
(91) Takeda, T.; Ozawa, M.; Akutagawa, T. Jumping Crystal of a Hydrogen-Bonded Organic Framework Induced by the Collective Molecular Motion of a Twisted pi System. *Angew Chem Int Ed Engl* **2019**, *58* (30), 10345-10352. DOI: 10.1002/anie.201905075.
(92) Fdez Galvan, I.; Vacher, M.; Alavi, A.; Angeli, C.; Aquilante, F.; Autschbach, J.; Bao, J. J.; Bokarev, S. I.; Bogdanov, N. A.; Carlson, R. K.; et al. OpenMolcas: From Source Code to Insight. *J Chem Theory Comput* **2019**, *15* (11), 5925-5964. DOI: 10.1021/acs.jctc.9b00532.
(93) Abadi, M.; Agarwal, A.; Barham, P.; Brevdo, E.; Chen, Z.; Citro, C.; Corrado, G. S.; Davis, A.; Dean, J.; Devin, M. Tensorflow: Large-scale machine learning on heterogeneous distributed systems. *arXiv preprint arXiv:1603.04467* **2016**.

View Article Online
DOI: 10.1039/D6SC00969G

## Data and code availability

- The ML-photodynamics simulation code is open-sourced and released at: https://github.com/mlcclab/PyRAI2MD-hiam.
- The NN models and initial conditions generated during this study are available at: https://doi.org/10.6084/m9.figshare.29294225.v1
- The complete training data and initial conditions can be requested from the corresponding author.